Monthly Notices
of the
ROYAL ASTRONOMICAL SOCIETY

MNRAS **429,** 398–422 (2013) doi:10.1093/mnras/sts344

A magnetic confinement versus rotation classification of massive-star magnetospheres

V. Petit,[1]⋆ S. P. Owocki,[2] G. A. Wade,[3] D. H. Cohen,[4] J. O. Sundqvist,[2] M. Gagné,[1] J. Maíz Apellániz,[5] M. E. Oksala,[6] D. A. Bohlender,[7] T. Rivinius,[8] H. F. Henrichs,[9] E. Alecian,[10] R. H. D Townsend,[11] A. ud-Doula[12] and the MiMeS Collaboration[12]

[1]*Department of Geology & Astronomy, West Chester University, West Chester, PA 19383, USA*
[2]*Department of Physics & Astronomy, University of Delaware, Bartol Research Institute, Newark, DE 19716, USA*
[3]*Department of Physics, Royal Military College of Canada, PO Box 17000, Stn Forces, Kingston, ON K7K 7B4, Canada*
[4]*Department of Physics & Astronomy, Swarthmore College, Swarthmore, PA 19081, USA*
[5]*Instituto de Astrofísica de Andalucía-CSIC, Glorieta de la Astronomía s/n, E-18008 Granada, Spain*
[6]*Astronomický ústav, Akademie věd České republiky, Fričova 298, CZ-251 65 Ondřejov, Czech Republic*
[7]*National Research Council of Canada, Herzberg Institute of Astrophysics, 5071 West Saanich Road, Victoria, BC V9E 2E7, Canada*
[8]*ESO – European Organization for Astronomical Research in the Southern Hemisphere, Casilla 19001, Santiago 19, Chile*
[9]*Astronomical Institute Anton Pannekoek, University of Amsterdam, Science Park 904, NL-1098 XH Amsterdam, the Netherlands*
[10]*LESIA, Observatoire de Paris, CNRS UMR 8109, UPMC, Université Paris Diderot, 5 place Jules Janssen, F-92190 Meudon, France*
[11]*Department of Astronomy, University of Wisconsin-Madison, 475 N Charter Street, Madison, WI 53706, USA*
[12]*Penn State Worthington Scranton, Dunmore, PA 18512, USA*

Accepted 2012 November 1. Received 2012 November 1; in original form 2012 October 2

ABSTRACT

Building on results from the Magnetism in Massive Stars (MiMeS) project, this paper shows how a two-parameter classification of massive-star magnetospheres in terms of the magnetic wind confinement (which sets the Alfvén radius R_A) and stellar rotation (which sets the Kepler co-rotation radius R_K) provides a useful organization of both observational signatures and theoretical predictions. We compile the first comprehensive study of inferred and observed values for relevant stellar and magnetic parameters of 64 confirmed magnetic OB stars with $T_{\rm eff} \gtrsim 16$ kK. Using these parameters, we locate the stars in the magnetic confinement–rotation diagram, a log–log plot of R_K versus R_A. This diagram can be subdivided into regimes of *centrifugal magnetospheres* (CM), with $R_A > R_K$, versus *dynamical magnetospheres* (DM), with $R_K > R_A$. We show how key observational diagnostics, like the presence and characteristics of Hα emission, depend on a star's position within the diagram, as well as other parameters, especially the expected wind mass-loss rates. In particular, we identify two distinct populations of magnetic stars with Hα emission: namely, slowly rotating O-type stars with narrow emission consistent with a DM, and more rapidly rotating B-type stars with broader emission associated with a CM. For O-type stars, the high mass-loss rates are sufficient to accumulate enough material for line emission even within the relatively short free-fall time-scale associated with a DM: this high mass-loss rate also leads to a rapid magnetic spindown of the stellar rotation. For the B-type stars, the longer confinement of a CM is required to accumulate sufficient emitting material from their relatively weak winds, which also lead to much longer spindown time-scales. Finally, we discuss how other observational diagnostics, e.g. variability of UV wind lines or X-ray emission, relate to the inferred magnetic properties of these stars, and summarize prospects for future developments in our understanding of massive-star magnetospheres.

Key words: circumstellar matter – stars: early-type – stars: fundamental parameters – stars: magnetic fields – stars: mass-loss – stars: rotation.

⋆ E-mail: vpetit@wcupa.edu

1 INTRODUCTION

Building on pioneering detections of strong (kG) fields in the chemically peculiar Ap and Bp stars (e.g. Babcock 1947; Borra & Landstreet 1980), new generations of spectropolarimeters have directly revealed large-scale, organized (often predominantly dipolar) magnetic fields ranging in dipolar strength[1] from order of 0.1 to 10 kG in several dozen OB stars (e.g. Donati et al. 2002, 2006a; Hubrig et al. 2006; Petit et al. 2008; Grunhut et al. 2009; Martins et al. 2010). In recent years, an observational consortium known as Magnetism in Massive Stars (MiMeS) has been carrying out surveys to detect new magnetic OB stars, while also monitoring known magnetic OB stars with high-resolution spectroscopy and polarimetry (Wade et al. 2011a). Concurrently, theoretical models (Townsend, Owocki & Groote 2005; Townsend, Owocki & ud-Doula 2007) and magnetohydrodynamical (MHD) simulations (ud-Doula & Owocki 2002; ud-Doula, Owocki & Townsend 2008, 2009) have explored the dynamical interaction of such fields with stellar rotation and mass loss, showing, for example, how suitably strong fields can channel the radiatively driven stellar wind outflow into a circumstellar *magnetosphere*. This paper aims now to provide an initial classification of the observed magnetospheric properties for a broad sample of magnetic massive stars.

The idea of a magnetosphere has been exploited to explain particular properties of some massive stars, for example the photometric light curve and Hα variations of the He-strong star σ Ori E (Landstreet & Borra 1978), the UV resonance line variations of magnetic Bp stars (Shore & Brown 1990), the X-ray properties of the O-type star θ^1 Ori C (Gagné et al. 2005), and the radio emission of Ap–Bp stars that correlates with the field strength (Linsky, Drake & Bastian 1992).

For a few specific stars, previous work has already shown some promising agreement between theoretical predictions and key observational characteristics. For example, the luminosity, hardness and rotational modulation of X-rays observed in the O-type star θ^1 Ori C all match well the X-rays computed in MHD simulations of magnetically confined wind shocks (MCWS), which result from the collision of the wind from opposite footpoints of closed magnetic loops in its $\sim$1 kG dipole field (Gagné et al. 2005). In the B2p star σ Ori E, the combination of its very strong ($\sim$10 kG) field and moderately fast (1.2-d period) rotation leads to the formation of a centrifugally supported magnetosphere with observed, rotationally modulated Balmer line emission reasonably well explained within the Rigidly Rotating Magnetosphere model (Townsend & Owocki 2005; Townsend et al. 2005). Most recently, Sundqvist et al. (2012) showed that, even in the very slowly rotating (537-d period) O-type star HD 191612, the magnetic confinement and transient, dynamical suspension of its strong wind mass loss lead to sufficient density to likewise match the observed rotationally modulated Balmer line emission.

Building on these results, along with those from the MiMeS observational survey, this paper compiles an exhaustive list of confirmed magnetic, hot OB stars, along with their physical, rotational and magnetic properties (Section 2). As a basis for organizing this compilation according to modelling predictions, we follow (Section 3) the two-parameter theoretical study of ud-Doula et al. (2008), which characterized MHD simulation results according to the strength of wind magnetic confinement (η_*) and fraction of stellar rotation to orbital speed at the stellar equatorial radius (W). These dimensionless parameters uniquely define associated characteristic radii, namely the Alfvén radius R_A and Kepler co-rotation radius R_K.

We show in particular (Section 4) that an associated log–log plot of known magnetic stars in the R_A-versus-R_K (or equivalently η_*-versus-W) plane, the *magnetic confinement–rotation diagram*, provides a particularly useful initial classification for interpreting the Hα properties of their associated magnetospheres. Furthermore, we also explore the UV and X-ray characteristics as potential additional proxies of magnetospheres (Section 5). We briefly review our main findings and conclusions in Section 6.

2 EXHAUSTIVE LIST OF MAGNETIC O-TYPE AND EARLY B-TYPE STARS

A central goal of this paper is to compile a comprehensive list of OB stars for which magnetic fields have been convincingly detected via the Zeeman effect, so that their magnetospheres can be classified.

The work here is done within the context of the MiMeS project (Wade et al. 2011a), which aims to expand the population of known magnetic stars, confirm the detection of poorly studied magnetic OB stars and provide a modern determination of their magnetic field characteristics. These goals are being achieved through Large Programme observing allocations at the Canada–France–Hawaii Telescope (CFHT), the Télescope Bernard-Lyot (TBL) and the European Southern Observatory (ESO) 3.6-m telescope to collect high-resolution, high signal-to-noise ratio spectropolarimetric observations of massive stars (see Wade et al. 2011a; Alecian et al. 2011; Oksala et al. 2012, respectively).

Table 1 lists our derived sample of 64 magnetic stars, ordered by spectral type and temperature. Column 1 gives the numerical identification (ID) we use in the figures. Column 2 gives the HD number or a SIMBAD-friendly[2] designation. A dagger indicates that a note for that particular star is available in Appendix A. Columns 3 and 4 give a commonly used designation and the spectral type, respectively. Column 5 indicates if the star is a known single- or double-line spectroscopic binary (SB1/2), slowly pulsating B-type star (SPB), β Cep-type pulsator (β Cep), or a Herbig Be star (HeBe). Table 2 compiles, for each star, the list of references where information can be found in the literature, or how it is derived from MiMeS observations or other archival data.

2.1 Sample selection

Magnetic fields in hot stars can be detected through the circular polarization induced in spectral lines by the Zeeman effect, using various types of instruments. The bulk of cooler magnetic ApBp stars were generally detected with first-generation photo-polarimeters, measuring for example the degree of polarization in the wings of a Balmer line (e.g. Borra & Landstreet 1980).

However, apart from a few strongly magnetic He-strong stars such as σ Ori E, the bulk of hot magnetic OB stars were detected with second generation instruments, such as the low-resolution ($R \simeq$ a few thousands) spectropolarimetry optics used in FORS 1 and 2 (VLT) and the high-resolution ($R \simeq$ a few tens of thousands) spectropolarimeters MUSICOS, ESPaDOnS, Narval and HARPSpol at the TBL, CFHT, TBL and ESO 3.6-m, respectively. These two classes of instruments differ in that low-resolution spectropolarimeters are

[1] In the following all field strengths will be given as dipolar, unless explicitly noted otherwise.

[2] http://simbad.u-strasbg.fr

Table 1. List of magnetic massive OB stars and their physical, rotational and magnetic properties.

ID	Star	Alt. name	Spec. type	Remark	$T_{\rm eff}$ (kK)	$\log g$ (cgs)	$\log(L_\star/L_\odot)$	R_* ($R_\odot$)	M_* ($M_\odot$)	P (d)	$v \sin i$ (km s^{-1})	$B_{\rm p}$ (kG)
(1)	(2)	(3)	(4)	(5)	(6)	(7)	(8)	(9)	(10)	(11)	(12)	(13)
1	HD 148937		O6 f?p		41 ± 2 [s]	4.0 ± 0.1	5.8 ± 0.1	15	60	7.0323	< 45	1.0
2	CPD -28 2561		O6.5 f?p		35 ± 2 [s]	4.0 ± 0.2	5.5 ± 0.2	14	43	70		> 1.7
3	HD 37022 †	θ^1 Ori C	O7 Vp	SB1	39 ± 1 [s]	4.1 ± 0.1	5.3 ± 0.1	9.9	45	15.424	24	1.1
4	HD 191612 †		O6 f?p-O8 fp	SB2	35 ± 1 [s]	3.5 ± 0.1	5.4 ± 0.2	14	30	537.2	< 60	2.5
5	NGC 1624-2		O6.5 f?cp-O8 f?cp		35 ± 2 [s]	4.0 ± 0.2	5.1 ± 0.2	9.7	34	158.0	< 3	> 20 [m]
6	HD 47129 †	Plaskett's star	O7.5 III	SB2	33 ± 2 [s]	4.1 ± 0.1	5.09 ± 0.04	10	56		305	> 2.8
7	HD 108		O8 f?p		35 ± 2 [s]	3.5 ± 0.2	5.7 ± 0.1	19	43	18000	< 50	> 0.50
8	ALS 15218 †	Tr16-22	O8.5 V		34 ± 2	4.0 ± 0.2	5.0 ± 0.1	9.0	28		25	> 1.5
9	HD 57682		O9 V		34 ± 1 [s]	4.0 ± 0.2	4.8 ± 0.2	7.0	17	63.571	15	1.7
10	HD 37742 †	ζ Ori Aa	O9.5 Ib	SB2	29 ± 1 [s]	3.2 ± 0.1	5.6 ± 0.1	25	40	7.0	110	0.060
11	HD 149438	τ Sco	B0.2 V		32 ± 1 [s]	4.0 ± 0.1	4.5 ± 0.1	5.6	11	41.033	5	0.20 [m]
12	HD 37061 †	NU Ori	B0.5 V	SB2	31.0 ± 0.5 [s]	4.2 ± 0.1	4.4 ± 0.1	5.7	19		225	0.65
13	HD 63425		B0.5 V		29 ± 1 [s]	4.0 ± 0.1	4.5 ± 0.4	6.8	17		< 10	0.46
14	HD 66665		B0.5 V		28 ± 1 [s]	3.9 ± 0.1	4.2 ± 0.5	5.5	9.0	21	< 10	0.67
15	HD 46328	ξ^1 CMa	B1 III	β Cep	27 ± 2 [s]	3.5 ± 0.2	4.6 ± 0.1	8.6	9.0	4.26	< 15	> 1.5
16	ALS 8988	NGC 2244 OI 201	B1	HeBe	27 ± 1 [s]	4.18 ± 0.06	4.05 ± 0.08	4.7	12		23	> 1.5
17	HD 47777	NGC 2264 83	B1 III	HeBe	27 ± 2 [s]	4.0 ± 0.2	4.1 ± 0.1	5.0	9.0		65	> 2.1
18	HD 205021 †	β Cep	B1 IV	SB2,β Cep	26 ± 1 [s]	3.7 ± 0.1	4.22 ± 0.08	6.5	12	12.00092	27	0.36
19	ALS 15211 †	Tr16-13	B1 V		26 ± 2	4.0 ± 0.2	4.0 ± 0.1	4.9	9.0			> 1.4
20	HD 122451 †	β Cen	B1	SB2,β Cep	25 ± 2	3.5 ± 0.4	4.4 ± 0.2 [p]	8.7	8.8		75	> 0.25
21	HD 127381	σ Lup	B1/B2 V		23 ± 1 [s]	4.0 ± 0.1	3.76 ± 0.06	4.8	9.0	3.0197	68	0.50
22	ALS 3694	NGC 6193 17	B1		20 ± 3	4.0 ± 0.4	3.7 ± 0.3 [p]	5.6	11		83	> 6.0
23	HD 163472	V 2052 Oph	B1/B2 V	β Cep	25 ± 1 [s]	4.2 ± 0.1	3.8 ± 0.1	4.1	10	3.638833	68	0.40
24	HD 96446 †	V 430 Car	B1 IVp/B2 Vp		21.6 ± 0.8 [s]	4.0 ± 0.1	3.6 ± 0.2	4.5	8.0	5.73	3	6.5
25	HD 66765		B1/B2 V		20 ± 2	3.9 ± 0.2	3.6 ± 0.2 [c]	5.3	7.5	1.61	100	> 2.1
26	HD 64740	HR 3089	B1.5 Vp		24 ± 1 [s]	4.0 ± 0.1	4.1 ± 0.3	6.3	11	1.33026	160	16
27	ALS 15956	Col 228 30	B1.5 V		23 ± 3	3.6 ± 0.2	4.3 ± 0.2 [c]	9.1	11			> 1.5
28	ALS 9522	NGC 6611 W601	B1.5 Ve	HeBe	22 ± 2 [s]	3.8 ± 0.3	4.0 ± 0.1	6.4	10		190	> 4.0
29	HD 36982	LP Ori	B1.5 Vp		22 ± 2	4.0 ± 0.2	3.1 ± 0.2 [p]	2.5	2.2		80	0.91
30	HD 37017 †	V 1046 Ori	B1.5-2.5 IV-Vp	SB2	21 ± 2	4.1 ± 0.2	3.4 ± 0.2	3.9	7.2	0.90119	90	> 6.0
31	HD 37479	σ Ori E	B2 Vp		23 ± 2	4.0 ± 0.2	3.6 ± 0.2 [p]	3.9	5.0	1.1908	170	9.6 [m]
32	HD 149277 †		B2 IV/V	SB2	22 ± 3	4.0 ± 0.4	4.0 ± 0.3 [p]	7.0	17		15	> 4.7
33	HD 184927	V 1671 Cyg	B2 Vp		22 ± 1 [s]	3.9 ± 0.1	3.6 ± 0.2	4.3	5.5	9.530	14	3.9 [m]
34	HD 37776 †	V 901 Ori	B2 Vp		22 ± 1	4.0 ± 0.1	3.5 ± 0.1	3.8	5.5	1.538756	95	15 [m]
35	HD 136504 †	ϵ Lup	B2 IV-V	SB2,β Cep	22 ± 2	4.0 ± 0.2	3.8 ± 0.2 [c]	5.3	8.6		42	> 0.60
36	HD 156424		B2 V		22 ± 3	4.0 ± 0.3	3.7 ± 0.4 [p]	4.8	8.5		15	> 0.65
37	HD 156324		B2 V		22 ± 3	4.0 ± 0.3	3.7 ± 0.4 [p]	5.1	9.4		60	> 1.8
38	HD 121743	ϕ Cen	B2 IV	β Cep	22 ± 3	4.0 ± 0.3	3.7 ± 0.2 [p]	4.7	8.0		80	> 0.53
39	HD 3360	ζ Cas	B2 IV	SPB	20.4 ± 0.9 [s]	3.8 ± 0.1	3.7 ± 0.2	5.9	8.3	5.37045	17	> 0.34
40	HD 186205 †		B2 Vp		20 ± 3	4.0 ± 0.2	3.5 ± 0.2 [c]	4.9	7.4		5	> 1.7
41	HD 67621		B2 IV		19 ± 3	4.0 ± 0.3	3.3 ± 0.2 [p]	4.1	6.2	3.59	20	> 0.90
42	HD 200775 †	V 3780 Cep	B2 Ve	SB2, HeBe	18 ± 2	3.4 ± 0.2	4.0 ± 0.3	10	10	4.328	26	1.0
43	HD 35912	HR 1820	B2 V		18 ± 1	4.0 ± 0.1	3.3 ± 0.3 [p]	4.4	7.2	0.89786	< 12	> 6.0
44	HD 66522		B2 III		18 ± 2	4.0 ± 0.4	3.3 ± 0.2 [p]	4.6	7.6		< 10	0.90
45	HD 182180	HR 7355	B2 Vn		17 ± 1 [s]	4.2 ± 0.2	3.0 ± 0.1	3.7	6.0	0.5214404	310	11
46	HD 55522	HR 2718	B2 IV/V		17.4 ± 0.4 [s]	4.2 ± 0.1	3.0 ± 0.1	3.3	5.5	2.729	70	> 2.6
47	HD 142184	HR 5907	B2 V		17 ± 1 [s]	4.3 ± 0.1	2.8 ± 0.1	3.1	5.5	0.50828	290	10
48	HD 58260 †		B3 Vp		20 ± 2	3.5 ± 0.2	4.1 ± 0.2 [c]	9.5	9.5		< 12	> 7.0
49	HD 36485 †	δ Ori C	B3 Vp	SB2	20 ± 2	4.0 ± 0.1	3.5 ± 0.1 [c]	4.5	7.1	1.47775	32	10
50	HD 208057 †	16 Peg	B3 V	SPB	19 ± 3	3.9 ± 0.2	3.6 ± 0.2 [c]	5.5	7.1	1.441	104	> 0.50
51	HD 306795	NGC 3766 MG170	B3 V		18 ± 2	3.9 ± 0.2	3.2 ± 0.3 [p]	4.1	4.3		65	> 5.0
52	HD 25558 †	40 Tau	B3 V	SPB	17 ± 2	4.0 ± 0.2	3.1 ± 0.2 [p]	3.9	5.5		28	> 0.15
53	HD 35298 †		B3 Vw		16 ± 2	3.8 ± 0.2	3.2 ± 0.2 [c]	5.5	5.6	1.85336	260	> 9.0
54	HD 130807	o Lup	B5		18 ± 2	4.1 ± 0.1	3.1 ± 0.1 [c]	3.5	5.7		25	> 2.0
55	HD 142990 †	V 913 Sco	B5 V		17 ± 2	4.2 ± 0.2	2.9 ± 0.2 [p]	3.1	5.7	0.97907	125	> 7.5
56	HD 37058 †	V 359 Ori	B3 VpC		17 ± 2	3.8 ± 0.2	3.5 ± 0.2 [c]	5.6	6.6	14.61	25	> 3.0
57	HD 35502 †		B5 V	SB2	16 ± 2	3.8 ± 0.2	3.3 ± 0.2 [c]	5.7	5.7	0.85	80	> 6.8
58	HD 176582	HR 7185	B5 IV		16 ± 1 [s]	4.0 ± 0.1	2.9 ± 0.1	3.6	4.7	1.581984	105	7.0
59	HD 189775	HR 7651	B5 V		16 ± 2	3.8 ± 0.2	3.2 ± 0.2 [c]	5.3	5.5	2.6048	85	> 4.5

Table 1 – *continued*

ID	Star	Alt. name	Spec. type	Remark	$T_{\rm eff}$ (kK)	$\log g$ (cgs)	$\log(L_\star/L_\odot)$	R_* ($R_\odot$)	M_* ($M_\odot$)	P (d)	$v \sin i$ (km s^{-1})	$B_{\rm p}$ (kG)
(1)	(2)	(3)	(4)	(5)	(6)	(7)	(8)	(9)	(10)	(11)	(12)	(13)
60	HD 61556 †	HR 2949	B5 V		15 ± 2	4.0 ± 0.3	2.6 ± 0.1 [p]	2.8	2.9	1.9093	70	4.0 [m]
61	HD 175362 †	Wolff's star	B5 V		15 ± 3	3.7 ± 0.2	3.2 ± 0.1 [c]	5.8	5.3	3.6738	35	> 21 [m]
62	HD 105382 †	HR 4618	B6 III		17 ± 2	4.0 ± 0.2	3.0 ± 0.2 [p]	3.6	4.8	1.285	90	2.3
63	HD 125823	a Cen	B7 IIIp		19 ± 2	4.0 ± 0.2	3.2 ± 0.1 [p]	3.6	4.7	8.812	15	> 1.3
64	HD 36526	V1099 Ori	B8 Vp		16 ± 3	4.0 ± 0.3	2.5 ± 0.3 [p]	2.4	2.0	1.5405		> 10

† Notes in Appendix.

Notes. Single- or double-lined spectroscopic binary (SB1-2), slowly pulsating B-type star (SPB), β Cep-type pulsator (β Cep), Herbig Be star (HeBe).

[s]Parameters determined from modern spectral modelling.

[p]Luminosity derived from our photometric calculations with BC.

[c]Luminosity derived from SED fitting with Chorizos.

[m]Higher multipole components.

Table 2. List of references for properties retrieved from the literature with superscript letters indicating the type of parameter. Superscript letters in Column 2 indicate information we inferred from MiMeS observations or other archival data, as indicated in the text.

ID	Star	Ref.	ID	Star	Ref.
(1)	(2)	(3)	(1)	(2)	(3)
1	HD 148937	Wade et al. (2012b)[srba]	32	HD 149277 [ra]	Bagnulo et al. (2006)[b]
		Fullerton (private communication)[u]			Landstreet et al. (2007)[s]
		Nazé, Zhekov & Walborn (2012b)[x]	33	HD 184927	Wade et al. (1997)[r]
2	CPD -28 2561	Barba et al. (MiMeS, in preparation)[srba]			Yakunin et al. (MiMeS, in preparation)[sbau]
3	HD 37022	Simón-Díaz et al. (2006)[s]	34	HD 37776	Landstreet et al. (2007)[s]
		Stahl et al. (2008)[ra]			Kochukhov et al. (2011)[b]
		Wade et al. (2006)[b]			Mikulášek et al. (2011)[r]
		Walborn & Nichols (1994)[u]			Shultz et al. (MiMeS, in preparation)[a]
		Stelzer et al. (2005)[x]			Shore & Brown (1990)[u]
4	HD 191612	Wade et al. (2011b)[srba]	35	HD 136504 [a]	Uytterhoeven et al. (2005)[sr]
		Fullerton (private communication)[u]			Shultz et al. (2012)[b]
		Nazé et al. (2007)[x]			Hubrig et al. (2009)[b]
5	NGC 1624-2	Wade et al. (2012a)[srbax]	36	HD 156424	Alecian (MiMeS, in preparation)[srba]
6	HD 47129	Linder et al. (2008)[srau]	37	HD 156324	Alecian (MiMeS, in preparation)[srba]
		Grunhut et al. (2012b)[b]	38	HD 121743	Wolff (1990)[s]
7	HD 108	Martins et al. (2010)[srb]			Alecian (MiMeS, in preparation)[rba]
		Marcolino et al. (2012)[au]			Grillo et al. (1992)[x]
		Nazé et al. (2004)[x]	39	HD 3360	Neiner et al. (2003)[srbau]
8	ALS 15218	Gagné et al. (2011)[s]			Oskinova et al. (2011)[x]
		Nazé et al. (2012a)[rba]	40	HD 186205	Zboril & North (2000)[r]
		Nazé et al. (2011)[x]			Grunhut (MiMeS private communication)[sba]
9	HD 57682	Grunhut et al. (2009)[sbaux]	41	HD 67621	Alecian et al. (MiMeS, in preparation)[srba]
		Grunhut et al. (2012c)[r]	42	HD 200775	Alecian et al. (2008a)[srb]
10	HD 37742	Bouret et al. (2008)[srba]			Hamaguchi, Yamauchi & Koyama (2005)[x]
		Kaper et al. (1996)[u]	43	HD 35912	Simón-Díaz (2010)[sa]
		Raassen et al. (2008)[x]			Bychkov, Bychkova & Madej (2005)[rb]
11	HD 149438 [a]	Simón-Díaz et al. (2006)[s]	44	HD 66522	Zboril et al. (1997)[s]
		Donati et al. (2006b)[rbu]			Leone, Catalano & Malaroda (1997)[s]
		Mewe et al. (2003)[x]			Alecian (MiMeS, in preparation)[rba]
12	HD 37061 [u]	Simón-Díaz et al. (2011)[sra]	45	HD 182180	Rivinius et al. (2012)[srba]
		Petit et al. (2008)[b]	46	HD 55522 [a]	Briquet et al. (2004)[sr]
		Stelzer et al. (2005)[x]			Briquet et al. (2007)[b]
13	HD 63425	Petit et al. (2011)[srbau]	47	HD 142184	Grunhut et al. (2012a)[srba]
14	HD 66665	Petit et al. (2011)[srbau]			Oskinova et al. (2011)[x]
15	HD 46328	Fourtune-Ravard et al. (2011)[srbau]	48	HD 58260	Bohlender (1989)[s]
		Oskinova et al. (2011)[x]			Cidale et al. (2007)[sb]
16	ALS 8988	Alecian et al. (2008b)[srb]			Pedersen (1979)[ra]
		Wang et al. (2008)[x]			Shore & Brown (1990)[u]
17	HD 47777	Alecian (private communication)[srb]	49	HD 36485	Leone et al. (2010)[srba]
		Nazé (2009)[x]			Shore & Brown (1990)[u]
18	HD 205021	Donati et al. (2001)[srbu]	50	HD 208057	Chauville et al. (2001)[s]
		Lefever et al. (2010)[s]			Henrichs et al. (2009)[rbau]
		Catanzaro (2008)[a]	51	HD 306795	McSwain (2008)[srb]
		Favata et al. (2009)[x]			McSwain et al. (2008)[a]

Table 2 – *continued*

ID (1)	Star (2)	Ref. (3)	ID (1)	Star (2)	Ref. (3)
19	ALS 15211	Gagné et al. (2011)^{s}	52	HD 25558 ^{b}	Lefever et al. (2010)^{sr}
		Nazé et al. (2012a)^{b}	53	HD 35298 ^{a}	Landstreet et al. (2007)^{s}
		Nazé et al. (2011)^{x}			Bychkov et al. (2005)^{rb}
20	HD 122451 ^{a}	Ausseloos et al. (2006) ^{s}			Yakunin et al. (2011)^{b}
		Alecian et al. (2011) ^{rb}	54	HD 130807	Alecian et al. (2011)^{srb}
		H. Henrichs (priv. com.)^{u}	55	HD 142990	Cidale et al. (2007)^{s}
		Raassen et al. (2005)^{x}			Bychkov et al. (2005)^{rb}
21	HD 127381	Henrichs et al. (2012)^{srbau}			Shore et al. (2004)^{au}
22	ALS 3694	Bagnulo et al. (2006)^{b}	56	HD 37058	Glagolevskij, Leushin & Chountonov (2007)^{s}
		Landstreet et al. (2007) ^{s}			Pedersen (1979)^{r}
		Huang & Gies (2006) ^{r}			Bychkov et al. (2005)^{rb}
23	HD 163472	Neiner et al. (2003b)^{su}			Ramírez et al. (2004)^{x}
		Neiner et al. (2012c)^{rb}	57	HD 35502	Landstreet et al. (2007)^{s}
		C. Neiner (priv. com.)^{a}			Romanyuk & Kudryavtsev (2008)^{b}
		Oskinova et al. (2011)^{x}			Bohlender et al. (in preparation)^{rba}
24	HD 96446	Neiner et al. (2012b)^{srba}			Grillo et al. (1992)^{x}
		Shore & Brown (1990)^{u}	58	HD 176582	Bohlender & Monin (2011)^{srba}
25	HD 66765	Cidale et al. (2007)^{s}	59	HD 189775	Lyubimkov et al. (2002)^{s}
		Alecian et al. (MiMeS, in preparation)^{rba}			Bohlender et al. (private communication)^{rb}
26	HD 64740	Bohlender & Landstreet (1990)^{sr}	60	HD 61556	Rivinius et al. (2003)^{r}
		Shore & Brown (1990)^{u}			Shultz et al. (in preparation)^{sba}
		Peralta et al. (MiMeS, in preparation)^{ba}	61	HD 175362	Leone & Manfre (1997)^{s}
		Drake et al. (1994)^{x}			Bychkov et al. (2005)^{rb}
27	ALS 15956	Bagnulo et al. (2006)^{sb}			Shore et al. (2004)^{au}
		Nazé et al. (2011)^{x}			Grillo et al. (1992)^{x}
28	ALS 9522	Alecian et al. (2008b)^{srba}	62	HD 105382	Briquet, Aerts & De Cat (2001)^{sra}
		Guarcello et al. (2012)^{x}			Alecian et al. (2011)^{b}
29	HD 36982 ^{u}	Wolff, Strom & Hillenbrand (2004)^{r}	63	HD 125823	Bohlender, Rice & Hechler (2010)^{srb}
		Petit & Wade (2012)^{sba}	64	HD 36526	Landstreet et al. (2007)^{s}
		Stelzer et al. (2005)^{x}			Bychkov et al. (2005)^{r}
30	HD 37017 ^{a}	Bolton et al. (1998)^{sr}			Romanyuk & Kudryavtsev (2008)^{b}
		Bohlender et al. (1987)^{b}			
		Shore & Brown (1990)^{u}			
		Oskinova et al. (2011)^{x}			
31	HD 37479	Hunger, Heber & Groote (1989)^{s}			
		Townsend et al. (2010)^{r}			
		Oksala et al. (2012)^{ba}			
		Shore & Brown (1990)^{u}			
		Sanz-Forcada, Franciosini & Pallavicini (2004)^{x}			

^{s} Stellar parameters, ^{r} Rotational parameters, ^{b} Magnetic field parameters.
^{a} Hα proxy, ^{u} UV proxy, ^{x} X-ray proxy.

only sensitive to the disc-integrated, brightness-weighted longitudinal field component, whereas high-resolution instruments can probe field configurations through the rotationally induced Doppler shifts within the resolved line profiles (see Donati & Landstreet 2009; Petit 2011).

We use the existing compilations of ApBp stars (e.g. Bychkov et al. 2005; Landstreet et al. 2007; Romanyuk & Kudryavtsev 2008) as well as an exhaustive review of the literature to identify hot stars with confirmed field detections, which we complement with new detections from the MiMeS project.

Some concerns have recently been raised about claimed magnetic detections (usually near the 3σ level) obtained with the FORS instruments that were not reproduced with other high-resolution instruments (see Silvester et al. 2009; Shultz et al. 2012). Bagnulo et al. (2012) performed an in-depth study of the complete set of FORS circular polarization measurements in the ESO archive, exploring the effect of various data reduction procedures and carefully considering all known sources of uncertainties. Using their new prescription for FORS data analysis, most of the claimed marginal detections were found to have very low significance, in agreement with the results from high-resolution instruments. They also provided updated longitudinal field values and new magnetic detection statuses for stars that were reported magnetic in the literature at the $<6\sigma$ level. We therefore base our selection on these new detection statuses for stars that were only detected with the FORS instruments.

It is worth noting that stars with chemical abundance peculiarities can have effective temperatures that do not reflect their spectral types, as the latter is determined from spectral morphology. In particular He-strong/weak stars, which form the majority of the cooler part of our sample, are identified by their unusually strong/weak He lines, lines that are the basic means to classify B-type stars. Given that photometric/spectral effective temperature determinations are not always readily available, it is therefore difficult to assess the completeness of our sample at the low-temperature boundary. We therefore consider all magnetic stars with spectral type B5 and earlier, as well as additional stars of later spectral type known to have effective temperatures greater than 16 kK. We believe the sample

at these temperatures (and above) to be a substantially complete representation of the currently known hot magnetic stars.

Although we consider a detailed review of the large sample of stars evaluated for inclusion in Table 1 beyond the scope of this work, two noteworthy objects require a brief mention. The first of these is the Be star ω Ori, reported to be magnetic by Neiner et al. (2003c) based on MuSiCoS longitudinal field measurements. Recently, Neiner et al. (2012a) have retracted this claim based on new ESPaDOnS and Narval measurements. The second is ζ Ori A, reported to be magnetic by Bouret et al. (2008). While no single observation of this star yields a significant magnetic detection, overall we consider the evidence presented by Bouret et al. (2008) to be sufficiently compelling that we retain this star in our list. Note that ζ Ori A occupies a unique position in the magnetic confinement–rotation diagram (see Section 3).

2.2 Physical parameters

Effective temperatures and surface gravities (Columns 6 and 7 of Table 1) were retrieved from the literature. An *s* superscript in Column 6 indicates stellar parameters that were determined by modern spectral modelling, with non local thermodynamic equilibrium (NLTE) model atmospheres such as CMFGEN, TLUSTY or FASTWIND for the hotter stars, or such as LTE ATLAS models with the polarized radiative transfer code ZEEMAN for the cooler stars (Kurucz 1979; Landstreet 1988; Hillier & Miller 1998; Wade et al. 2001; Lanz & Hubeny 2003; Puls et al. 2005). For the other stars, temperatures and gravities were generally derived from photometry combined with spectral type calibrations. Some details are given in the notes of Appendix A in cases where significant discrepancies were found in the literature values or when we had to estimate $\log g$ from the luminosity class.

When modern spectral modelling is available, we use the literature value for the luminosity, radius and mass (Columns 8–10). The luminosity is generally obtained through a distance estimate and photometry, and the spectroscopic mass is derived from the surface gravity and radius, unless a better estimate is available from a binary orbit.

For most of the remaining stars, marked with superscript *p* or *c* in Column 8, we derive the luminosity from photometry (see Section 2.2.1) using tabulated bolometric corrections (BC), or using the spectral energy distribution (SED) fitting code CHORIZOS (Maíz-Apellániz 2004) for stars with sufficient photometric data.

In Fig. 1, we locate the magnetic OB stars on the Hertzsprung–Russell (HR) diagram. The symbol shapes represent the O-type stars (circles), B-type stars hotter than 22 kK (squares), those between 22 kK and 19 kK (triangles) and those that are cooler than 19 kK (pentagons), and known Herbig Be stars (HeBe; diamonds). The luminosity classes are colour coded. The labels refer to the identification numbers in Column 1 of Table 1.

The position of the spectral types, from the calibrations of Martins et al. (2005) for the O-type stars and de Jager & Nieuwenhuijzen (1987) for the B-type stars, is indicated on the dark grey line that runs approximately mid-way between the zero-age main sequence and the terminal-age main sequence; the main sequence itself is shown by the light grey shaded area (from the galactic evolutionary tracks of Brott et al. 2011).

2.2.1 *Luminosity derivation*

For each star in our sample without modern spectral modelling, Table 3 gathers visual magnitudes and colours (Columns 3–5) in the Johnson *UBV* system, from the compilations of Mermilliod (2006) and Reed (2005).[3] We also provide *RJHK* magnitudes (Columns 6–9) from the NOMAD catalogue (Zacharias et al. 2005), which will be used below for SED fitting with CHORIZOS.

For all these stars, we derive the luminosity using BC and extinction (A_V) evaluated from the intrinsic colour $(B-V)_0$. The results are compiled in Table 4. The distance modulus (DM; Column 4) is estimated using either *Hipparcos* parallax measurements or a distance estimate from an association with a stellar cluster. The *Hipparcos* distances are corrected for Lutz-Kelker-type effects (Lutz & Kelker 1973) using the technique described by Maíz-Apellániz (2001, 2005) updated to the new reduction of the *Hipparcos* data (van Leeuwen 2007) by Maíz Apellániz, Alfaro & Sota (2008).

The theoretical BC and $(B-V)_0$ (Columns 5 and 6) are determined from a smooth interpolation of the grids provided by Martins et al. (2005), and Martins & Plez (2006) for the O-type stars and Lanz & Hubeny (2007) for the B-type stars. We use an extinction $R_V = 3.1$ to derive the extinction $A_V = R_V\,E(B-V)$ (Column 7). The absolute visual magnitude ($M_V = V - A_V - \mathrm{DM}$), the bolometric magnitude ($M_{\rm bol} = M_V + \mathrm{BC}$) and the luminosity [$\log(L_\star/\mathrm{L}_\odot) = (M_{\rm bol,\,\odot} - M_{\rm bol})/2.5$] are given in Columns 8 to 10.

With a typical uncertainty of 2000 K in $T_{\rm eff}$ and 0.3 dex in $\log g$, we estimate an uncertainty of 0.2 and 0.02 mag in BC and $(B-V)_0$, respectively. Given the wide range of R_V often encountered in the literature for OB stars, we adopt a conservative error in A_V of 0.25 mag. In most cases, BC, A_V and DM contribute equally to the uncertainty, leading to 0.2–0.3 dex for the luminosity. In five cases (ID: 36, 37, 40, 53 and 57) the luminosity error estimate from the BC method is more than 0.4 dex, given the large uncertainty in distance.

For the stars with a complete set of *UBVRJHK* photometry, we perform SED fitting using the Bayesian (spectro)photometric code CHORIZOS. The results are presented in Table 5. In the latest CHORIZOS version, the user can select distance to be an independent parameter by applying atmosphere models (TLUSTY for OB stars) calibrated in luminosity with the help of Geneva stellar evolution tracks (excluding rotational effects). The parameters of such models are the logarithmic distance (Column 3), the extinction (here fixed at $R_{5495} = 3.1$[4]), the reddening (transformed to A_V in Column 4), the effective temperature (here fixed to the literature estimate) and the luminosity class. The distance range has been left relatively wide around the *Hipparcos* or cluster-estimated value and the luminosity class prior probability was based on the gravity estimates used for the BC approach (Column 3 of Table 4) with an interval of 1.5σ. From these fitted values, we can derive an estimate of the surface gravity (Column 5), the evolutionary mass (Column 6) and the luminosity (Column 7).

Good fits to the photometry are achieved for the 13 stars displayed in Table 5, leading to better estimates of their luminosity (especially for the two stars with the largest uncertainty with the BC approach). Poorer fits were obtained for the remaining nine stars with complete

[3] As no Johnson *UBV* measurements are available for HD 61556 (ID 60) and HD 306795 (ID 51), we use the Strömgren photometry from Hauck & Mermilliod (1998) with the transformation given by Turner (1990).

[4] The extinction law is defined by the monochromatic quantity $R_{5495} \equiv A_{5495}/E(4405-5495)$ instead of a band-integrated one such as $R_V \equiv A_V/E(B-V)$, because the former depends only on the properties of the dust while the latter also depends on the input SED and the amount of dust present along the line of sight. See Maíz Apellániz (2012) for details.

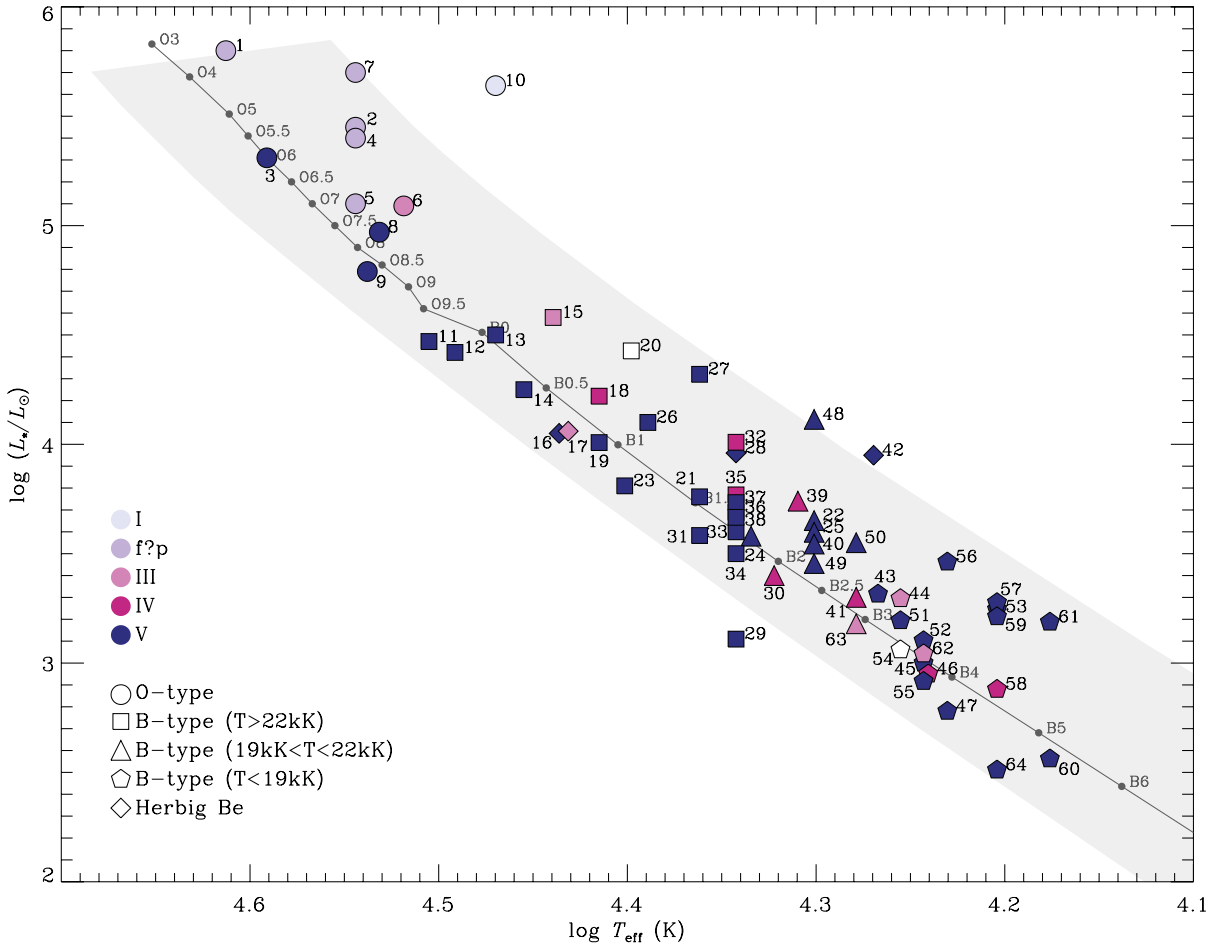

Figure 1. Location of the magnetic stars in the HR diagram. The labels refer to ID sequence number listed in Column 1 of Table 1. The various symbol shapes represent effective temperature ranges and colours denote luminosity classes, as indicated in the legend. The shaded region shows the main sequence, from zero-age main sequence to terminal-age main sequence (from the galactic evolutionary tracks of Brott et al. 2011). The grey line shows the mid-way main sequence with spectral type calibrations from Martins, Schaerer & Hillier (2005) for O-type stars and de Jager & Nieuwenhuijzen (1987) for B-type stars.

photometry. Incompatibility between optical and near-IR photometry, probably due to near-IR excess, could be a possible cause of the discrepancy. Therefore, for the stars with good fits, we use the luminosity, gravity and mass derived from CHORIZOS. For the remaining stars, we opt for the BC luminosity determination.

2.3 Rotational and magnetic parameters

Monitoring of the disc-integrated longitudinal field variations provides a natural and direct way to determine rotational periods for magnetic stars (in the context of the Oblique Rotator Model; e.g. Stibbs 1950). Photometric and spectral variability associated with the magnetic field also provide a convenient and easy way to determine periods, even though some ambiguity can exist between, for example, short rotational periods and long pulsation periods.

In Table 1, Column 11 gives the rotational period in days. When no period is available we use the measured $v \sin i$ (Column 12) as a lower limit to the equatorial velocity. In two cases (ALS 15211, ID 19; ALS 15956, ID 27), no $v \sin i$ measurements are available due to a lack of high-resolution spectra. These stars would be prime candidates for further monitoring.

In four cases (HD 96446, HD 136504, HD 58260 and HD 37058; ID 24, 35, 48 and 56) more than one period is reported in the literature. In these cases, we use the longest period for a lower limit on the equatorial velocity. We provide the magnetospheric calculations for the alternative periods in the notes of Appendix A.

Column 13 gives the estimated polar strength ($B_{\rm p}$) of the surface dipole in kilogauss. When only longitudinal magnetic measurements are available, we use a value of three times the strongest longitudinal field measurement (corresponding to a conservative limb-darkening coefficient[5] of 0.6), setting a lower limit on the dipolar field strength. A superscript *m* in Column 13 indicates stars that are known to possess a magnetic field with a significant contribution from multipole components higher than a simple dipole.

3 TWO-PARAMETER CLASSIFICATION OF MAGNETOSPHERES

3.1 Alfvén radius $R_{\rm A}$ versus Kepler co-rotation radius $R_{\rm K}$

The high luminosity of massive stars drives powerful, high-speed stellar winds. MHD simulation studies (e.g. ud-Doula & Owocki

[5] In the case of a dipolar field, the dipole strength can be expressed as $B_{\rm p} \geq 4\frac{15-5\epsilon}{15+\epsilon}|\langle B_z\rangle|_{\rm max}$, where ϵ is the limb-darkening coefficient and $|\langle B_z\rangle|_{\rm max}$ is the maximum of the disc-integrated longitudinal field variation (Preston 1967).

Table 3. Photometry of magnetic stars without modern spectral modelling (Section 2.2.1).

ID	Star	V	$(B-V)$	$(U-B)$	R	J	H	K
		±0.01 mag	±0.01 mag	mag	±0.02 mag	±0.02 mag	±0.02 mag	±0.02 mag
(1)	(2)	(3)	(4)	(5)	(6)	(7)	(8)	(9)
20	HD 122451 †	0.61	− 0.24					
22	ALS 3694	10.38	0.33	−0.55 ± 0.02	10.26	9.62	9.49	9.47
25	HD 66765	6.62	− 0.16	−0.8 ± 0.2	6.69	6.89	7.01	7.01
27	ALS 15956	10.80	0.05	−0.69 ± 0.02	10.70	10.62	10.64	10.66
29	HD 36982	8.45	0.13	−0.57 ± 0.02	8.42	7.74	7.64	7.47
31	HD 37479	6.66	− 0.18	−0.87 ± 0.01	6.40	6.97	6.95	6.95
32	HD 149277 †	8.38	0.04	−0.658 ± 0.009	8.43	8.26	8.26	8.28
35	HD 136504 †	3.37	− 0.18	−0.74 ± 0.02	3.44	3.99*	3.93*	4.13*
36	HD 156424	8.72	0.06					
37	HD 156324	8.75	0.10					
38	HD 121743	3.82	− 0.22					
40	HD 186205 †	8.53	0.05	−0.60 ± 0.02	8.50	8.40	8.48	8.48
41	HD 67621	6.33	− 0.20	−0.802 ± 0.004	6.41	6.73	6.86	6.84
43	HD 35912	6.41	− 0.18					
44	HD 66522	7.20	0.05	−0.624 ± 0.005	7.19	7.03	7.02	7.01
48	HD 58260 †	6.74	− 0.13	−0.756 ± 0.006	6.79	6.98	7.11	7.12
49	HD 36485 †	6.85	− 0.16	−0.72 ± 0.01	6.92	7.17	7.23	7.28
50	HD 208057 †	5.07	− 0.17	−0.7 ± 0.1	5.16	5.39	5.49	5.54
51	HD 306795	10.62	0.02					
52	HD 25558 †	5.32	− 0.08	−0.57 ± 0.01	5.35	5.48	5.58	5.53
53	HD 35298 †	7.89	− 0.14	−0.6 ± 0.2	7.94	8.12	8.17	8.27
54	HD 130807	4.32	− 0.15	−0.62 ± 0.01	4.38	4.78*	4.72	4.73
55	HD 142990 †	5.43	− 0.09	−0.653 ± 0.003	5.46	5.58	5.67	5.65
56	HD 37058 †	7.30	− 0.13	−0.79 ± 0.02	7.23	7.60	7.73	7.75
57	HD 35502 †	7.35	− 0.04	−0.54 ± 0.04	7.32	7.39	7.42	7.43
59	HD 189775	6.14	− 0.19	−0.66 ± 0.02	6.20	6.46	6.53	6.64
60	HD 61556 †	4.78	− 0.14					
61	HD 175362 †	5.37	− 0.15	−0.7 ± 0.1	5.43	5.62	5.66	5.68
62	HD 105382 †	4.46	− 0.16	−0.68 ± 0.01	4.51	5.12	4.95	4.87
63	HD 125823	4.37	− 0.19					
64	HD 36526	8.31	− 0.11					

* Because of their brightness, these stars have uncertainties of ±0.24 mag according to the 2MASS specifications.

2002; ud-Doula et al. 2008) show that the overall net effect of a large-scale, dipole magnetic field in diverting such a wind can be well characterized by a single *wind magnetic confinement parameter*,

$$\eta_* \equiv \frac{B_{\rm eq}^2\, R_*^2}{\dot{M}_{B=0}\, V_\infty}\,, \tag{1}$$

where $B_{\rm eq} = B_{\rm p}/2$ is the field strength at the magnetic equatorial surface radius R_*, and $\dot{M}_{B=0}$ and V_∞ are the fiducial mass-loss rate and terminal speed that the star *would have* in the *absence* of any magnetic field.

This confinement parameter sets the scaling for the ratio of the magnetic to wind kinetic energy density. For a dipole field, the r^{-6} radial decline of magnetic energy density is much steeper than the r^{-2} decline of the wind's mass and energy density; this means the wind always dominates beyond the *Alfvén radius* $R_{\rm A}$ (ud-Doula et al. 2008), given by the approximate general scaling,

$$\frac{R_{\rm A}}{R_*} \approx 0.3 + (\eta_* + 0.25)^{1/4}\,. \tag{2}$$

Magnetic loops extending above $R_{\rm A}$ are drawn open by the wind, while those with an apex below $R_{\rm A}$ remain closed. Indeed, the trapping of wind upflow from opposite footpoints of closed magnetic loops leads to strong collisions that may form X-ray emitting, MCWSs (Babel & Montmerle 1997a,b, see Section 5.2). In models with negligible rotation, the post-shock material eventually cools and falls back on to the star, leading to a relatively complex, dynamic pattern of infall and wind outflow (see e.g. lower row of fig. 9 of ud-Doula et al. 2008, also Fig. 2).

For the simple 2D axisymmetric case of a magnetic dipole that is aligned with a star's rotation axis, ud-Doula et al. (2008) extended these MHD simulation studies to explore the additional effect of stellar rotation. They found it convenient to cast results in terms of the ratio of the rotation speed $V_{\rm rot}$ to orbital speed $V_{\rm orb}$ at the equatorial surface radius R_*,

$$W \equiv \frac{V_{\rm rot}}{V_{\rm orb}} = \frac{\omega R_*}{\sqrt{GM_*/R_*}}\,, \tag{3}$$

where the latter equality expresses this ratio in terms of the angular rotation frequency ω, with M_* the stellar mass. To avoid the complications associated with a rotationally distorted, oblate stellar surface, ud-Doula et al. (2008) restricted their simulations to cases with $W \leq 0.5$. But if we associate R_* with the *actual equatorial* radius for the given rotation rate ω, then even for more rapid, near-critical rotation, W simply compares the star's equatorial rotation speed to the speed $V_{\rm orb}$ needed to reach the Keplerian orbit near this equatorial surface.[6]

[6] For critical rotation ($W = 1$), $R_* = 3R_{\rm p}/2$, where $R_{\rm p}$ is the *fixed* polar radius. In terms of the associated critical rotational frequency $\omega_{\rm crit} \equiv \sqrt{8GM/27R_{\rm p}^3}$, one can alternatively define a critical rotation ratio $\Omega \equiv \omega/\omega_{\rm crit}$. We then

Table 4. Luminosity determination based on BC and extinction from intrinsic colours (Section 2.2.1).

ID	Star	$\log g$ (cgs)	DM (mag)	BC ($\pm$0.2 mag)	$(B-V)_0$ ($\pm$0.02 mag)	A_V ($\pm$0.25 mag)	M_V (mag)	M_{bol} (mag)	$\log(L_\star/L_\odot)$
(1)	(2)	(3)	(4)	(5)	(6)	(7)	(8)	(9)	(10)
20	HD 122451 †	3.5 ± 0.4		-2.48			-3.8 ± 0.5 *	-6.3 ± 0.5	4.4 ± 0.2
22	ALS 3694	4.0 ± 0.4	11.2 ± 0.6 [c]	-1.98	-0.18	1.57	-2.4 ± 0.7	-4.4 ± 0.8	3.7 ± 0.3
25	HD 66765	4.0 ± 0.2	8.4 ± 0.4	-1.98	-0.18	0.06	-1.9 ± 0.5	-3.8 ± 0.6	3.4 ± 0.2
27	ALS 15956	4.0 ± 0.4	12.8 ± 0.6 [c]	-2.32	-0.20	0.78	-2.8 ± 0.7	-5.1 ± 0.7	3.9 ± 0.3
29	HD 36982	4.0 ± 0.2	8.3 ± 0.2 [c]	-2.21	-0.19	1.01	-0.8 ± 0.3	-3.0 ± 0.4	3.1 ± 0.2
31	HD 37479	4.0 ± 0.2	8.5 ± 0.4 [c]	-2.31	-0.20	0.07	-1.9 ± 0.5	-4.2 ± 0.5	3.6 ± 0.2
32	HD 149277 †	4.0 ± 0.4	10.7 ± 0.6 [c]	-2.21	-0.19	0.72	-3.1 ± 0.7	-5.3 ± 0.7	4.0 ± 0.3
35	HD 136504 †	4.0 ± 0.2	6.1 ± 0.3	-2.21	-0.19	0.04	-2.7 ± 0.4	-5.0 ± 0.4	3.9 ± 0.2
36	HD 156424	4.0 ± 0.3	10 ± 1 [c]	-2.21	-0.19	0.78	-2 ± 1	-4 ± 1	3.7 ± 0.4
37	HD 156324	4.0 ± 0.3	10 ± 1 [c]	-2.21	-0.19	0.92	-2 ± 1	-5 ± 1	3.7 ± 0.4
38	HD 121743	4.0 ± 0.3	6.03 ± 0.07	-2.21	-0.19	0.00	-2.2 ± 0.3	-4.4 ± 0.4	3.7 ± 0.2
40	HD 186205 †	4.0 ± 0.2	14 ± 1	-1.98	-0.18	0.70	-6 ± 1	-8 ± 1	5.1 ± 0.5
41	HD 67621	4.0 ± 0.3	8.0 ± 0.2	-1.85	-0.17	0.00	-1.7 ± 0.3	-3.5 ± 0.5	3.3 ± 0.2
43	HD 35912	4.0 ± 0.1	8.2 ± 0.7	-1.78	-0.16	0.00	-1.8 ± 0.7	-3.5 ± 0.7	3.3 ± 0.3
44	HD 66522	4.0 ± 0.4	8.3 ± 0.4	-1.71	-0.16	0.64	-1.8 ± 0.4	-3.5 ± 0.5	3.3 ± 0.2
48	HD 58260 †	3.8 ± 0.3	9.7 ± 0.5	-1.97	-0.18	0.15	-3.2 ± 0.6	-5.1 ± 0.6	3.9 ± 0.3
49	HD 36485 †	4.2 ± 0.2	8.4 ± 0.7 [c]	-1.99	-0.18	0.06	-1.6 ± 0.7	-3.6 ± 0.8	3.3 ± 0.3
50	HD 208057 †	3.9 ± 0.2	6.4 ± 0.1	-1.85	-0.17	0.00	-1.4 ± 0.3	-3.2 ± 0.5	3.2 ± 0.2
51	HD 306795	3.9 ± 0.2	11.6 ± 0.6 [c]	-1.71	-0.16	0.55	-1.5 ± 0.7	-3.2 ± 0.7	3.2 ± 0.3
52	HD 25558 †	4.0 ± 0.2	6.5 ± 0.1	-1.64	-0.15	0.21	-1.4 ± 0.3	-3.0 ± 0.4	3.1 ± 0.2
53	HD 35298 †	4.0 ± 0.3	12 ± 1	-1.41	-0.14	0.00	-4 ± 1	-5 ± 1	3.9 ± 0.5
54	HD 130807	4.2 ± 0.2	5.5 ± 0.2	-1.72	-0.15	0.00	-1.2 ± 0.3	-2.9 ± 0.4	3.1 ± 0.2
55	HD 142990 †	4.2 ± 0.2	6.16 ± 0.09	-1.64	-0.15	0.17	-0.9 ± 0.3	-2.6 ± 0.4	2.9 ± 0.2
56	HD 37058 †	3.8 ± 0.2	8.5 ± 0.4 [c]	-1.71	-0.16	0.09	-1.3 ± 0.5	-3.0 ± 0.6	3.1 ± 0.2
57	HD 35502 †	4.0 ± 0.3	9 ± 2	-1.41	-0.14	0.30	-2 ± 2	-4 ± 2	3.3 ± 0.8
59	HD 189775	4.0 ± 0.3	6.9 ± 0.1	-1.41	-0.14	0.00	-0.8 ± 0.3	-2.2 ± 0.4	2.8 ± 0.1
60	HD 61556 †	4.0 ± 0.3	5.2 ± 0.2	-1.24	-0.12	0.00	-0.4 ± 0.3	-1.7 ± 0.4	2.6 ± 0.1
61	HD 175362 †	4.0 ± 0.3	5.60 ± 0.08	-1.24	-0.12	0.00	-0.2 ± 0.3	-1.5 ± 0.4	2.5 ± 0.1
62	HD 105382 †	4.0 ± 0.2	5.7 ± 0.2	-1.64	-0.15	0.00	-1.2 ± 0.3	-2.9 ± 0.4	3.0 ± 0.2
63	HD 125823	4.0 ± 0.2	5.73 ± 0.06	-1.85	-0.17	0.00	-1.4 ± 0.3	-3.2 ± 0.4	3.2 ± 0.1
64	HD 36526	4.0 ± 0.3	8.4 ± 0.7 [c]	-1.41	-0.14	0.08	-0.1 ± 0.7	-1.5 ± 0.8	2.5 ± 0.3

* From the SB2 analysis of Ausseloos et al. (2006).
[c] Distance estimates from associations with stellar clusters (*Hipparcos* otherwise).

Table 5. Luminosity determination based on SED fitting with CHORIZOS (Section 2.2.1).

ID	Star	DM (mag)	A_V (mag)	$\log g$ (cgs)	M_* ($M_\odot$)	$\log(L_\star/L_\odot)$
(1)	(2)	(3)	(4)	(5)	(6)	(7)
25	HD 66765	8.6 ± 0.5	0.21 ± 0.02	3.9 ± 0.2	7.5 ± 0.6	3.6 ± 0.2
27	ALS 15956	13.6 ± 0.6	0.92 ± 0.02	3.6 ± 0.2	11 ± 1	4.3 ± 0.2
35	HD 136504 †	5.6 ± 0.5	0.19 ± 0.04	4.0 ± 0.2	8.6 ± 0.7	3.8 ± 0.2
40	HD 186205 †	9.9 ± 0.5	0.75 ± 0.02	4.0 ± 0.2	7.4 ± 0.6	3.5 ± 0.2
48	HD 58260 †	10.0 ± 0.5	0.24 ± 0.01	3.5 ± 0.2	9 ± 1	4.1 ± 0.2
49	HD 36485 †	8.6 ± 0.4	0.19 ± 0.02	4.0 ± 0.1	7.1 ± 0.4	3.5 ± 0.1
50	HD 208057 †	7.2 ± 0.5	0.12 ± 0.02	3.9 ± 0.2	7.1 ± 0.6	3.6 ± 0.2
53	HD 35298 †	9.7 ± 0.6	0.12 ± 0.02	3.8 ± 0.2	5.6 ± 0.5	3.2 ± 0.2
54	HD 130807	5.3 ± 0.3	0.13 ± 0.01	4.1 ± 0.1	5.7 ± 0.2	3.1 ± 0.1
56	HD 37058 †	9.4 ± 0.5	0.07 ± 0.03	3.8 ± 0.2	6.6 ± 0.5	3.5 ± 0.2
57	HD 35502 †	8.9 ± 0.6	0.40 ± 0.01	3.8 ± 0.2	5.7 ± 0.5	3.3 ± 0.2
59	HD 189775	7.9 ± 0.5	0.00 ± 0.02	3.8 ± 0.2	5.5 ± 0.5	3.2 ± 0.2
61	HD 175362 †	7.2 ± 0.4	0.08 ± 0.01	3.7 ± 0.2	5.3 ± 0.4	3.2 ± 0.1

In a magnetic star, torques from the magnetic field on any wind outflow can maintain rigid-body co-rotation up to roughly the Alfvén radius, so that the azimuthal speed of the confined wind plasma *increases* with radius as $v_\phi = V_{rot} r/R_*$. The outward centrifugal force from such rigid-body rotation will balance the inward force of gravity at the *Kepler corotation radius*,

$$R_K \equiv \left(\frac{GM}{\omega^2}\right)^{1/3} = W^{-2/3} R_* \,. \quad (4)$$

find $W = \Omega(2R_*/3R_p)$, with $R_*/R_p = 3\cos[(\cos^{-1}[\Omega] + \pi)/3]/\Omega$ (Collins & Harrington 1966).

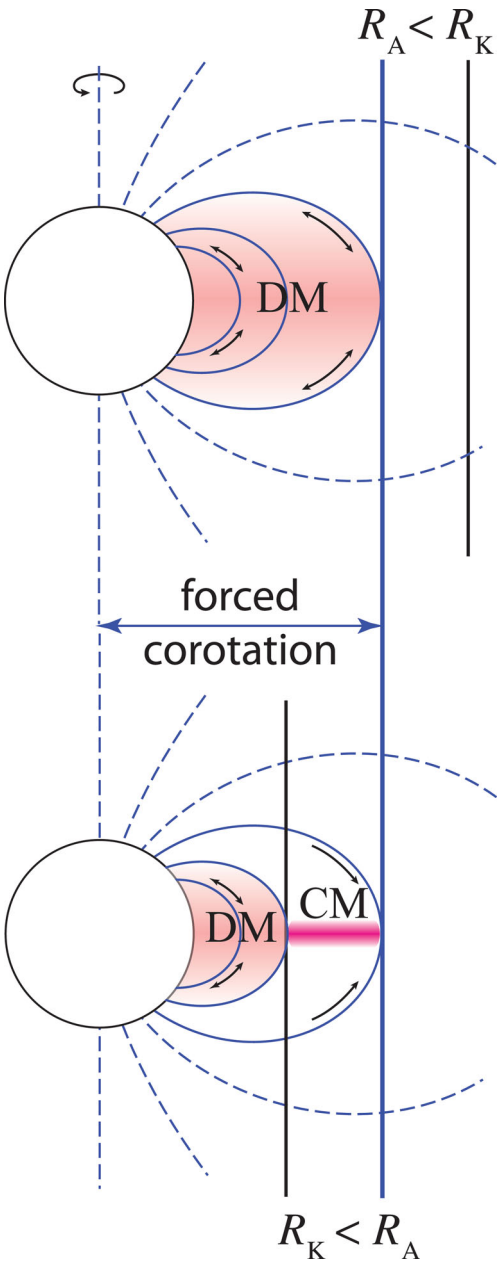

Figure 2. Sketch of the regimes for dynamical versus centrifugal magnetospheres (DM versus CM). The top panel illustrates the case of a slowly rotating star with the Kepler radius beyond the Alfvén radius ($R_K > R_A$); the lack of centrifugal support means that trapped material falls back to the star on a dynamical time-scale, forming a DM, with colour illustrating the rough time-averaged distribution of density. The lower panel is for a star with more rapid rotation and $R_K < R_A$, leading then to a region between these radii where a net outward centrifugal force against gravity is balanced by the magnetic tension of closed loops; this allows material to build up to the much higher density of CM.

Together the two parameters η_* and W thus define the relative locations of the Alfvén and Kepler radii with respect to the equatorial radius.

3.2 Dynamical versus centrifugal magnetospheres

For the simple case of field-aligned rotation, ud-Doula et al. (2008) carried out an extensive MHD simulation parameter study varying both W and η_*. For $\eta_* < 1$, the field exerts only a modest perturbation on the wind; but for $\eta_* > 1$, outflow near the magnetic equator is trapped within the Alfvén radius by closed magnetic loops, forming a wind-fed circumstellar *magnetosphere*. It was found that the dynamical evolution of this trapped magnetospheric material depends crucially on the rotation parameter W, and specifically on the relative magnitude of the associated Kepler versus the Alfvén radii.

In a simplified, schematic form, Fig. 2 here illustrates that, depending on the relative positions of R_K versus R_A, regions of trapped equatorial material can be alternatively characterized as forming a *dynamical* versus *centrifugal* magnetosphere (DM versus CM). As sketched in the upper panel of Fig. 2, for slowly rotating stars with $R_A < R_K$, material trapped in closed magnetic loops falls back to the star on a dynamical time-scale, forming a DM (Sundqvist et al. 2012). In contrast, the lower panel shows that, for the more rapidly rotating case with $R_A > R_K$, material caught in the region between R_A and R_K is centrifugally supported against infall, and so builds up to a much denser CM (for a given fiducial mass-loss rate). Even for such rapid rotators, the inner regions below R_K again have the infall of a DM, but the plasma density, and thus any circumstellar emission, is much lower than that of the CM region.

Indeed, since the much longer confinement time allows material to accumulate to high density even if the feeding by the wind mass flux is weak, such a CM can exhibit rotationally modulated line emission even in the relatively low luminosity, but strongly magnetic Bp stars, so long as the stellar rotation is sufficient to give $R_K < R_A$ (Townsend & Owocki 2005; Townsend et al. 2005). For slowly rotating magnetic stars with a DM, accumulating sufficiently high density plasma for line emission requires a much stronger wind to overcome the dynamical time-scale leakage of infall back on to the star. For the luminous, slowly rotating magnetic O-type star HD 191612 (ID 4), Sundqvist et al. (2012) showed that the emission from its wind-fed DM matches its observed Hα emission quite well.

The transition from stars with a pure DM to those with a CM occurs near $R_K = R_A$; from equations (2) and (4), the associated transition value W_t for the rotation fraction is

$$W_t = \left[0.3 + (\eta_* + 0.25)^{1/4}\right]^{-3/2} , \quad (5)$$

which in the strong confinement limit, $\eta_* \gg 1$, simply requires $W_t \approx \eta_*^{-3/8}$.

Fig. 3 plots our sample of magnetic stars in the magnetic confinement–rotation diagram, a log–log plane with R_K/R_* increasing downward on the ordinate versus R_A/R_* increasing to the right along the abscissa. As detailed in the next section (Section 3.3), the placement of the individual stars depends on inference of the relevant parameters that set the magnetic confinement η_* (noted on the top axis) and rotation fraction W (on the right axis). The vertical line at $\eta_* = 1$ ($R_A/R_* \approx 1.3$) separates weakly magnetized winds at the far left from the broad domain of stars with significant magnetospheres, with the diagonal line separating the stars with a CM to the upper right from those with just a DM to the lower left. As detailed in Section 3.4, the additional upper and right axes refer to associated stellar spindown properties, namely the stellar spindown time-scale (τ_J) and the maximum spindown age ($t_{s,\,max}$), respectively. Stars above the horizontal dotted line have a maximum spindown age $t_{s,\,max}$ that is less than one spindown time τ_J.

3.3 Calculation of magnetospheric parameters

In this section, we determine the magnetospheric parameters described in Section 3.1 for all the stars in the sample. Table 6

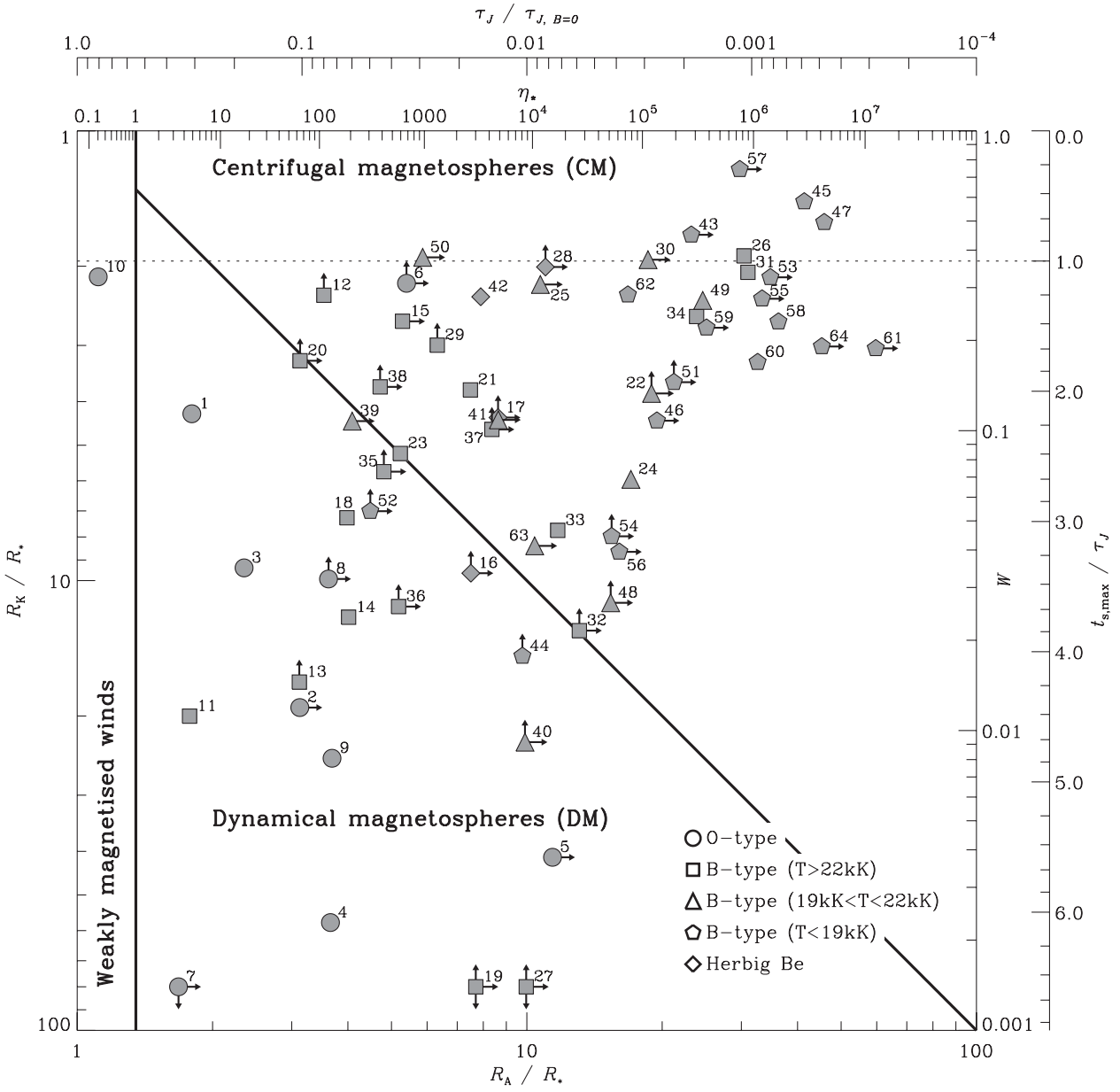

Figure 3. Location of magnetic massive stars in the magnetic confinement–rotation diagram; a log–log plot with the Kepler radius R_K increasing downwards and the Alfvén radius R_A increasing to the right. The right and upper axes give, respectively, the corresponding rotation fraction W and magnetic confinement parameter η_*. The solid lines separate the magnetosphere domains of weakly magnetized winds (with $\eta_* < 1$), DM with $R_A < R_K$ and CM with $R_A > R_K$ as defined in Section 3.2. The additional upper and right axes give, respectively, the corresponding spindown time-scale τ_J (normalized by the value in a non-magnetized wind) and maximum spindown age $t_{s,\,max}$ (normalized by the spindown time and therefore the number of spindown e-folds), as defined in Section 3.4. Stars above the dashed line have a maximum spindown age less than one spindown time. As in Fig. 1, the symbol shapes denote spectral type, and the numbers correspond to the ID in Column 1 of Table 1. The three downward arrows indicate two stars (ALS 15211, ID 19; ALS 15956, ID 27) for which no $v \sin i$ measurement is available (e.g. $W > 0$), and HD 108 (ID 7) for which $R_K \sim 500 R_*$.

compiles our calculations of $\eta_\star$, R_A/R_*, W and R_K/R_* (equations 1 to 4) in Columns 4 to 7.

3.3.1 *Wind momentum*

To compute η_* and R_A from equations (1) and (2), we need, in addition to the stellar radius and surface magnetic field, estimates of the wind mass-loss rate $\dot{M}_{B=0}$ and terminal speed V_∞. Simulation models define the confinement in terms of wind properties a star *would* have if it had *no* magnetic field. Therefore instead of making empirical estimates of the wind properties of each magnetic star (which are in any case difficult to obtain; see Sundqvist et al. 2012; Grunhut et al. 2012c), we derive theoretical values based on inferred stellar parameters applied to radiation line-driven wind theory.

Following standard theory, we take the wind terminal speed V_∞ to scale with the star's effective surface escape speed,

$$V_{\rm esc} \equiv \left(\frac{2GM_*(1-\Gamma_e)}{R_*} \right)^{1/2}, \qquad (6)$$

Table 6. List of magnetospheric parameters, magnetic spindown properties, and Hα, UV and X-ray proxies.

ID	Star	Remark	W	R_K/R_*	η_*	R_A/R_*	τ_J (Myr)	$t_{s,\,max}$ (Myr)	$\log(R_A/R_K)$	Hα	UV	$\log(L_X/L_\star)$
(1)	(2)	(3)	(4)	(5)	(6)	(7)	(8)	(9)	(10)	(11)	(12)	(13)
1	HD 148937		1.1 e-1	4.3	4.9	1.8	0.82	1.8	− 0.37	var em	var	− 6.6
2	CPD -28 2561		1.2 e-2	19	> 6.4 e1	> 3.1	< 0.92	< 4.1	> − 0.79	var em		
3	HD 37022 †	SB1	3.5 e-2	9.4	1.8 e1	2.4	3.1	10	− 0.60	var em	per	− 5.6
4	HD 191612 †	SB2	2.3 e-3	57	1.3 e2	3.7	0.38	2.3	− 1.20	var em	var	− 6.0
5	NGC 1624-2		3.8 e-3	41	> 1.5 e4	> 11	< 0.24	< 1.4	> − 0.56	var em		− 6.6
6	HD 47129 †	SB2	> 3.1 e-1	< 2.2	> 6.8 e2	> 5.4	< 4.1	< 4.8	> 0.39	em	var	− 5.6
7	HD 108		8.3 e-5	526	> 3.5	> 1.7	< 0.90	< 8.5	> − 2.50	var em	var	− 6.2
8	ALS 15218 †		> 3.2 e-2	< 9.9	> 1.2 e2	> 3.6	< 3.1	< 10	> − 0.44	em		− 6.3
9	HD 57682		8.1 e-3	24	1.3 e2	3.7	2.2	10	− 0.83	var em	var	− 6.3
10	HD 37742 †	SB2	3.3 e-1	2.1	2.0 e-1	1.1	3.9	4.4	− 0.28	var em	abs	− 6.7
11	HD 149438		1.1 e-2	20	4.6	1.8	21	97	− 1.05	var abs	per	− 6.3
12	HD 37061 †	SB2	> 2.8 e-1	< 2.3	1.1 e2	3.5	27	< 35	> 0.18	abs	stab abs	− 6.9
13	HD 63425		> 1.5 e-2	< 16	6.3 e1	3.1	22	< 93	> − 0.73	stab abs	var	
14	HD 66665		2.4 e-2	12	1.9 e2	4.0	12	46	− 0.48	stab abs	var	
15	HD 46328	β Cep	2.3 e-1	2.7	> 6.2 e2	> 5.3	< 1.6	< 2.3	> 0.30	em	em	− 6.8
16	ALS 8988	HeBe	> 3.3 e-2	< 9.6	> 2.7 e3	> 7.5	< 23	< 78	> − 0.11	HeBe		− 8.8
17	HD 47777	HeBe	> 1.1 e-1	< 4.3	> 4.8 e3	> 8.6	< 8.9	< 19	> 0.30	HeBe		− 6.9
18	HD 205021 †	SB2,β Cep	5.1 e-2	7.3	1.8 e2	4.0	43	128	− 0.26	abs	per	− 7.2
19	ALS 15211 †				> 3.0 e3	> 7.7	< 17		> -2.29			− 7.8
20	HD 122451 †	SB2,β Cep	> 1.7 e-1	< 3.2	> 6.5 e1	> 3.1	< 14	< 26	> − 0.02	abs	stab abs	− 7.3
21	HD 127381		1.4 e-1	3.8	2.7 e3	7.5	127	254	0.30	stab abs	var	
22	ALS 3694		> 1.3 e-1	< 3.8	> 1.2 e5	> 18	< 3.0	< 6.1	> 0.69			
23	HD 163472	β Cep	8.4 e-2	5.2	5.9 e2	5.2	157	390	0.00	abs	per	− 8.6
24	HD 96446 †		6.9 e-2	6.0	7.9 e4	17	2.2	5.8	0.46	stab abs	em	
25	HD 66765		3.1 e-1	2.2	> 1.2 e4	> 10	< 4.8	< 5.6	> 0.69	stab abs		
26	HD 64740		3.8 e-1	1.9	8.2 e5	30	1.7	1.6	1.20	var em	per	− 7.3
27	ALS 15956				> 8.8 e3	> 9	< 7.4		> -2.14			− 6.8
28	ALS 9522	HeBe	> 3.5 e-1	< 2.0	> 1.3 e4	> 11	< 1.3	< 1.4	> 0.74	HeBe		− 7.3
29	HD 36982		> 1.9 e-1	< 3.0	1.3 e3	6.3	8.6	< 14	> 0.32	stab abs	stab abs	− 7.8
30	HD 37017 †	SB2	3.7 e-1	1.9	> 1.1 e5	> 18	< 3.7	< 3.6	> 0.98	var em	per	− 7.8
31	HD 37479		3.4 e-1	2.1	8.9 e5	31	4.6	5.0	1.18	var em	per	− 5.9
32	HD 149277 †	SB2	> 2.2 e-2	< 12	> 2.7 e4	> 13	< 2.6	< 10	> 0.01	abs		
33	HD 184927		4.7 e-2	7.7	1.7 e4	11	1.7	5.2	0.18	stab abs	per	
34	HD 37776 †		2.4 e-1	2.6	3.1 e5	23	0.68	0.97	0.96	var em	per	
35	HD 136504 †	SB2,β Cep	> 7.3 e-2	< 5.7	> 4.2 e2	> 4.8	< 12	< 32	> − 0.08	abs	abs	
36	HD 156424		> 2.6 e-2	< 11	> 5.7 e2	> 5.2	< 15	< 55	> − 0.34	var em		
37	HD 156324		> 1.0 e-1	< 4.6	> 4.2 e3	> 8.4	< 5.9	< 13	> 0.26	var em		
38	HD 121743	β Cep	> 1.4 e-1	< 3.7	> 3.8 e2	> 4.7	< 18	< 35	> 0.10	abs	abs	− 7.2
39	HD 3360	SPB	1.1 e-1	4.4	> 2.1 e2	> 4.1	< 19	< 43	> − 0.03	abs	per	− 7.8
40	HD 186205 †		> 9.1 e-3	< 22	> 8.5 e3	> 9.9	< 6.9	< 32	> − 0.36	stab abs		
41	HD 67621		1.1 e-1	4.4	> 4.9 e3	> 8.6	< 22	< 49	> 0.29	stab abs	abs	
42	HD 200775 †	SB2, HeBe	2.8 e-1	2.3	3.3 e3	7.9	3.6	4.6	0.53	HeBe		− 6.3
43	HD 35912		4.5 e-1	1.7	> 2.8 e5	> 23	< 4.1	< 3.3	> 1.13	abs		
44	HD 66522		> 1.8 e-2	< 14	8.1 e3	9.8	30	< 124	> − 0.18	abs		
45	HD 182180		5.8 e-1	1.4	2.9 e6	41	4.5	2.5	1.46	var em	abs	
46	HD 55522		1.1 e-1	4.4	> 1.4 e5	> 19	< 21	< 48	> 0.64	abs		
47	HD 142184		5.0 e-1	1.6	4.3 e6	45	9.5	6.7	1.46	var em		− 6.7
48	HD 58260 †		> 2.7 e-2	< 11	> 5.2 e4	> 15	< 0.29	< 1.1	> 0.14	abs	em	
49	HD 36485 †	SB2	2.7 e-1	2.4	3.5 e5	24	1.6	2.1	1.01	var em	var	
50	HD 208057 †	SPB	3.8 e-1	1.9	> 9.6 e2	> 5.9	< 18	< 18	> 0.49	abs	abs	
51	HD 306795		> 1.5 e-1	< 3.6	> 1.9 e5	> 21	< 2.8	< 5.5	> 0.77	abs		
52	HD 25558 †	SPB	> 5.4 e-2	< 7.0	> 3.1 e2	> 4.5	< 185	< 542	> − 0.19			
53	HD 35298 †		3.2 e-1	2.1	> 1.4 e6	> 34	< 1.7	< 1.9	> 1.22	stab abs		
54	HD 130807		> 4.4 e-2	< 8.0	> 5.3 e4	> 15	< 20	< 64	> 0.29			
55	HD 142990 †		2.8 e-1	2.4	> 1.2 e6	> 33	< 9.3	< 12	> 1.15	var em	per	
56	HD 37058 †		3.9 e-2	8.6	> 6.2 e4	> 16	< 3.7	< 11	> 0.27			
57	HD 35502 †	SB2	7.4 e-1	1.2	> 7.5 e5	> 29	< 2.1	< 0.61	> 1.39	var em		− 6.0
58	HD 176582		2.3 e-1	2.7	1.7 e6	36	6.7	9.9	1.14	var em		
59	HD 189775		2.2 e-1	2.7	> 3.8 e5	> 25	< 3.8	< 5.7	> 0.96			
60	HD 61556 †		1.7 e-1	3.3	1.1 e6	32	14	26	1.00	stab abs		

Table 6 – *continued*

ID	Star	Remark	W	R_K/R_*	η_*	R_A/R_*	τ_J (Myr)	$t_{s,\,max}$ (Myr)	$\log(R_A/R_K)$	Hα	UV	$\log(L_X/L_\star)$
(1)	(2)	(3)	(4)	(5)	(6)	(7)	(8)	(9)	(10)	(11)	(12)	(13)
61	HD 175362 †		1.9 e-1	3.0	> 1.2 e7	> 59	< 0.74	< 1.2	> 1.29	stab abs	var	− 6.3
62	HD 105382 †		2.8 e-1	2.3	7.4 e4	16	13	16	0.86	abs		− 6.8
63	HD 125823		4.1 e-2	8.4	> 1.0 e4	> 10	< 14	< 47	> 0.09	var abs	per	
64	HD 36526		1.9 e-1	3.0	> 4.1 e6	> 45	< 3.9	< 6.4	> 1.18			

† Notes in Appendix.

where $\Gamma_e \equiv \kappa_e L/4\pi GM_* c$ is the Eddington parameter for electron scattering opacity κ_e. For the order-unity ratio V_∞/V_{esc}, we use the factors recommended by Vink, de Koter & Lamers (2000, 2001) (based on the empirical study of Lamers, Snow & Lindholm 1995), which declines abruptly from 2.6 to 1.3 from the hot to cool side of the so-called 'bi-stability' jump at $T_{eff} \approx 25\,000$ K (see below).

For mass-loss rates, we also use the recipe given by Vink et al. (2000, 2001), assuming solar metallicity for all stars. This predicts an associated strong mass-loss increase of nearly an order of magnitude from the hot to cool side of this bi-stability jump, because iron recombination makes available more efficient driving-lines and so produces an increase in the line force. But note that, whereas the expected decrease in V_∞ over this bi-stability jump is empirically quite well established, this predicted increase in $\dot{M}_{B=0}$ is not yet observationally confirmed (e.g. Markova & Puls 2008).

For comparison, we therefore also compute mass-loss rates based on the standard (finite-disc-corrected) Castor, Abbott & Klein (1975, hereafter CAK) scaling. Using the notation from Gayley (1995), this can be written in the form

$$\dot{M}_{B=0,\mathrm{CAK}} = \frac{1}{(1+\alpha_{\mathrm{eff}})^{1/\alpha_{\mathrm{eff}}}} \frac{\alpha_{\mathrm{eff}}}{1-\alpha_{\mathrm{eff}}} \frac{L_\star}{c^2} \left(\frac{\bar{Q}\Gamma_e}{1-\Gamma_e} \right)^{-1+1/\alpha_{\mathrm{eff}}}, \quad (7)$$

where we adopt $\bar{Q} = 1000$ and $\alpha_{\mathrm{eff}} \approx 0.55$ for the full sample to represent the normalization and effective power-exponent of the line opacity distribution, where the latter has been adjusted to account for ionization effects (Puls, Springmann & Lennon 2000), and is in good agreement with the observationally inferred value for non-magnetic O-type stars (Repolust, Puls & Herrero 2004).

The left-hand panel of Fig. 4 compares the two mass-loss rate values for our full sample of magnetic massive stars, while the right-hand panel illustrates the shift in the confinement–rotation diagram resulting from switching between the two scalings.

For the hotter O-type stars the CAK scaling agrees quite well with the Vink et al. recipe, and, because of the weak $R_A \sim \dot{M}_{B=0}^{-1/4}$ dependence, this translates to a negligible shift in the confinement–rotation diagram. Of course, this comparison only reflects uncertainties due to different theoretical mass-loss descriptions. But recent multi-wavelength spectroscopic studies aiming to derive mass-loss rates in the O-type star domain typically yield rates that deviate from the Vink et al. prescription only by factors of ∼2–3, if small-scale wind inhomogeneities ('clumping') are adequately accounted for (e.g. Sundqvist et al. 2011; Najarro, Hanson & Puls 2011; Bouret et al. 2012), and, as illustrated by Fig. 4, such discrepancies barely affect stellar positions in the confinement–rotation diagram.

For B-type stars, however, mass-loss rate differences are generally much larger, an order of magnitude or more near the bi-stability jump. Empirical mass-loss determinations for B-type dwarfs (which comprise most of our magnetic sample) are difficult at most, but studies of B-type supergiants have found a decrease in wind momentum compared to the theoretical Vink et al. predictions for the complete low-temperature region (Markova & Puls 2008). Further deviations from theoretical wind momentum of similar magnitude have also been observed for some late O-type stars with so-called weak winds (for an overview see Puls, Vink & Najarro 2008).

Even with the weak $\dot{M}_{B=0}^{-1/4}$ scaling, the shift in R_A associated with these large deviations can approach 0.3 dex. For other quantities, such as the stellar spindown time, which scales as $R_A^2 \sim 1/\sqrt{\dot{M}_{B=0}}$, there can be a substantial change, by a factor of several, for different mass-loss values near and below the bi-stability region, as discussed further in Section 3.4.

In summary, these relatively large systematic differences in the adopted mass-loss rate will be an important concern for performing detailed modelling of magnetosphere signatures for individual stars. However, it can be seen from Fig. 4 (right) that despite these large differences, the overall appearance of the rotation–confinement diagram is not much affected and the basic, qualitative classification results presented here are quite robust against errors in the wind parameters. To maintain a uniform standard, all the presented magnetosphere parameter values in Table 6 are based on the Vink et al. scalings.

3.3.2 *Rotational oblateness*

As mentioned in Section 3.1, the calculation of the Alfvén and Kepler radii requires the actual equatorial radius of the star, in principle accounting for any rotationally induced oblateness. In practice, a 15 per cent oblateness requires $\Omega \approx 0.8$, equivalent to $W = 0.6$, and so except for the most rapid rotators, the difference between the polar and equatorial radii is generally much smaller than the uncertainty in the radius determination. In our sample, only three stars have a period short enough for oblateness to become potentially significant. For HD 182180 (ID 45) and HD 142184 (ID 47), we use the equatorial radii derived by Rivinius et al. (2012) and Grunhut et al. (2012a) from spectral analysis including the oblateness. As no such analysis is available for HD 35502 (ID 57), we use the radius derived from the Stefan–Boltzmann equation.

For simplicity, we ignore the effect of gravity darkening on the wind driving from the stellar surface. For aligned rotators, the wind feeding the equatorial magnetosphere originates from mid-latitudes, where gravity darkening is weaker. For non-aligned rotators, the magnetosphere will have a complex 3D structure that requires detailed modelling for each case. But in general terms, the maximum density occurs near R_K along the line defined by the *intersection* between the magnetic and rotational equators (Townsend & Owocki 2005; Townsend et al. 2005). In this context, the relative confinement and centrifugal support of the such magnetospheres should be well characterized by the Alfvén and Kepler radius relative to the star's *equatorial* radius, accounting for any rotational oblateness.

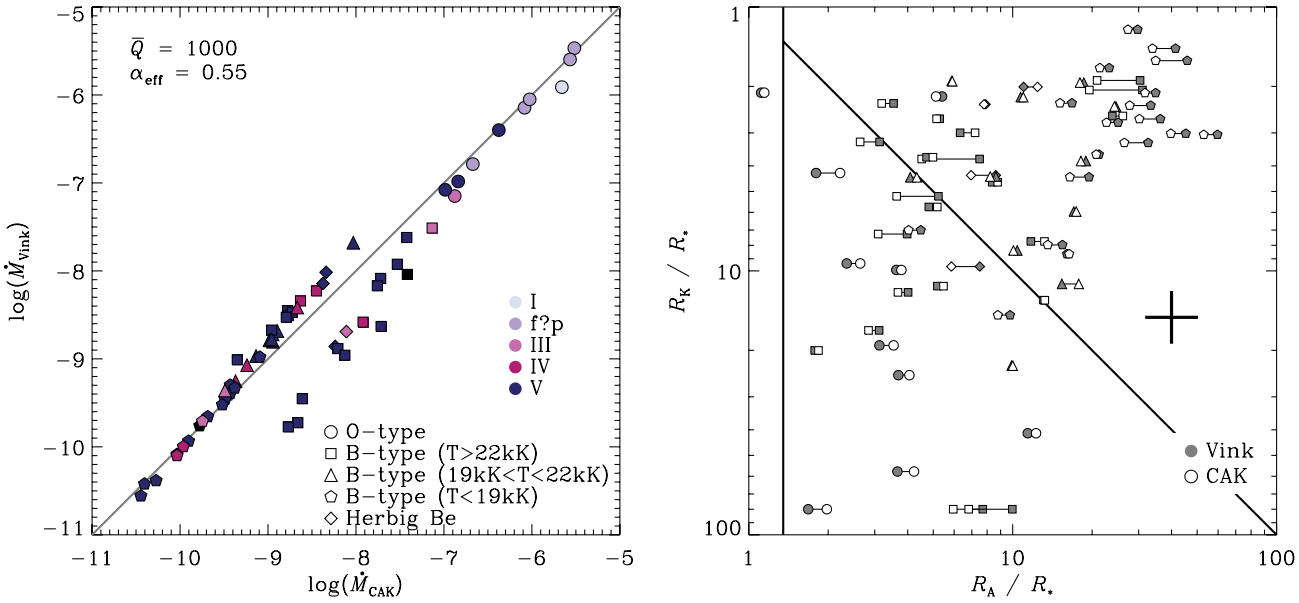

Figure 4. Left: comparison between the mass-loss rate calculations by Vink et al. (2000, 2001) and the CAK scaling law described in Section 3.3.1. Note the large change in mass-loss over the bi-stability jump in the Vink et al. rates. Right: shift in the Alvén radius from switching between the Vink et al. rates (filled symbols) and the CAK scaling law (empty symbols). The error bar in the lower right represents uncertainty in $R_{\rm K}$ and $R_{\rm A}$ estimated from the propagation of typical uncertainty in the stellar parameters *only* (∼25 per cent). The uncertainty in $R_{\rm A}$ is in fact dominated by systematics in the mass-loss rate determinations. However, the relative position in the magnetic confinement–rotation diagram, and hence the magnetospheric classification, is not too sensitive to these systematics, as described in Section 3.3.1.

3.3.3 Uncertainties in Kepler and Alfvén radii

Let us now explore the effect of stellar parameter uncertainty on the position of the stars in the confinement–rotation diagram. As the radius and mass of the stars are generally derived from $T_{\rm eff}$, $\log(L_\star/{\rm L}_\odot)$ and $\log g$, we propagate the uncertainty on these quantities, assuming they are independent.

The Kepler radius can be expressed as

$$\frac{R_{\rm K}}{R_*} \propto \frac{g^{1/3} T_{\rm eff}^{3/2}}{L_\star^{1/6} \omega^{2/3}}. \tag{8}$$

In general, the rotational periods are accurate at 1–2 per cent, so their uncertainty can be neglected. The quantities $T_{\rm eff}$, $\log g$ and $\log(L_\star/{\rm L}_\odot)$ have typical uncertainties of 10 per cent, 0.2 dex and 0.25 dex, respectively. From equation (8), they contribute 15, 15 and 10 per cent uncertainties to $R_{\rm K}$, for a total uncertainty of 23 per cent. Fig. 5 shows a histogram of the Kepler radius uncertainty distribution (grey shade) for our sample, confirming that the mean uncertainty is around 25 per cent. A corresponding vertical error bar is shown in the confinement–rotation diagram in Fig. 4 (right).

For the error propagation in the Alfvén radius, we follow the CAK scaling (for fixed $\alpha_{\rm eff} = 0.55$), for the dependence of wind momentum on stellar parameters (equations 6 and 7),

$$\dot{M}_{B=0} V_\infty \propto \frac{T_{\rm eff}^{2.24} L_\star^{1.25}}{g^{0.31}}. \tag{9}$$

With the typical uncertainties quoted above, $T_{\rm eff}$, $\log g$ and $\log(L_\star/{\rm L}_\odot)$ contribute, respectively, 22, 14 and 72 per cent uncertainties to the wind momentum, for a total uncertainty of 76 per cent. This uncertainty from stellar parameters is much smaller than

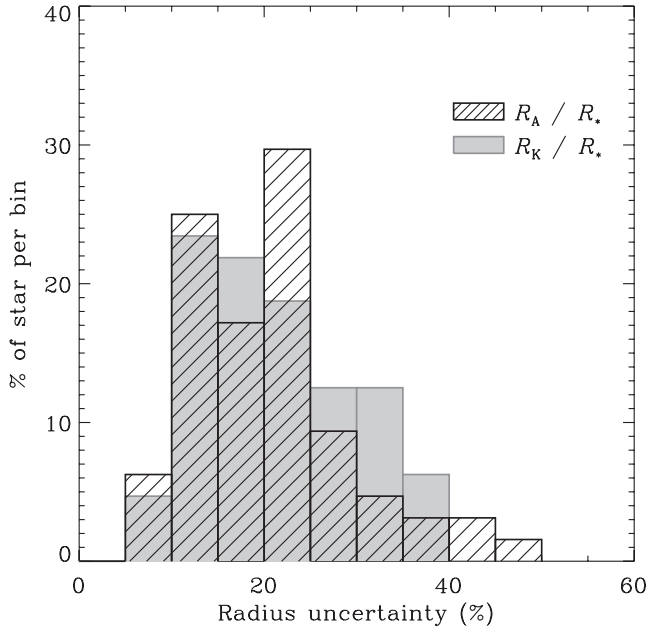

Figure 5. Distribution of uncertainties in our determination of the Kepler radius (shaded) and the Alvén radius (hatched), estimated by propagating the uncertainty on the stellar parameters [$T_{\rm eff}$, $\log(L_\star/{\rm L}_\odot)$ and $\log g$].

that associated with the systematics discussed in Section 3.3.1. As such, we estimate the total uncertainty in $R_{\rm A}$ through the scaling,

$$\frac{R_{\rm A}}{R_*} \propto \frac{B_{\rm p}^2 L_\star^{1/4}}{T_{\rm eff} (\dot{M}_{B=0} V_\infty)^{1/4}}. \tag{10}$$

As a large fraction of our sample has only lower limits on the dipole field strength, let us ignore for now its contribution to the uncertainty. Again with the uncertainties quoted above, $T_{\rm eff}$ and $\log(L_\star/{\rm L}_\odot)$ contribute 10 and 14 per cent uncertainties, whereas $\dot{M}_{B=0}V_\infty$ contributes 20 per cent uncertainty, for a total uncertainty in $R_{\rm A}$ of 26 per cent. Fig. 5 presents the uncertainty distribution attributed to the stellar parameters for $R_{\rm A}$ (hashed histogram) with a mean value again confirming the above estimate. One can see that the corresponding horizontal error bar in the confinement–rotation diagram of Fig. 4 (right) is smaller than the systematic uncertainty associated with the theoretical mass-loss rate determination.

Moreover, since the dipolar field strength is generally constrained with an accuracy of ∼30 per cent, it would only contribute a 15 per cent uncertainty to $R_{\rm A}$, again much smaller than the systematic uncertainty from the wind momentum.

3.4 Spindown time and spindown age

Let us next turn to considering the rotational evolution for our sample of magnetic massive stars. The angular momentum loss rate from a magnetized wind can be written in terms of the mass-loss rate, the Alfvén radius $R_{\rm A}$, and the stellar rotation frequency $\omega = V_{\rm rot}/R_*$ (Weber & Davis 1967; ud-Doula et al. 2009),

$$\dot{J} \approx \frac{2}{3}\dot{M}_{B=0}\omega R_{\rm A}^2 \,. \tag{11}$$

The associated time-scale for magnetic-wind-induced spindown of the stellar angular momentum $J = I\omega$ can then be written in the form

$$\tau_{\rm J} \equiv \frac{J}{\dot{J}} \approx \frac{3}{2}\frac{f M_* R_*^2 \omega}{\dot{M}_{B=0}R_{\rm A}^2\omega} = \frac{3}{2} f \tau_{\rm M}\left(\frac{R_*}{R_{\rm A}}\right)^2 ,$$
$$= \tau_{{\rm J},B=0}\left(\frac{R_*}{R_{\rm A}}\right)^2 , \tag{12}$$

where $\tau_{\rm M} \equiv M_*/\dot{M}_{B=0}$ is a characteristic mass-loss time-scale, and $\tau_{{\rm J},\,B=0}$ defines the spindown time in the case of no magnetic field (i.e. $R_{\rm A} = R_*$). The star's moment of inertia $I = f M_* R_*^2$ can be evaluated from the radius of gyration $\beta = f^{1/2}$ tabulated from internal structure models such as Claret (2004). If we assume for simplicity a fixed radius R_* and moment of inertia factor $f \approx 0.1$, as well as a constant angular momentum loss rate $\dot{J}$, then the stellar rotational period P will simply increase exponentially with age t from its initial value P_o,

$$P(t) = P_o {\rm e}^{t/\tau_{\rm J}} \,. \tag{13}$$

We can then use equation (13) to define a star's spindown *age*, $t_{\rm s}$, in terms of the spindown time $\tau_{\rm J}$, and its inferred present-day critical rotation fraction $W = P_{\rm orb}/P$ relative to its initial rotation fraction W_o at age $t = 0$,

$$\frac{t_{\rm s}}{\tau_{\rm J}} = \ln W_o - \ln W \,. \tag{14}$$

Taking the initial rotation to be critical, $W_o = 1$, yields a simple upper limit to the spindown age,

$$t_{\rm s,max} = \tau_{\rm J}\ \ln(1/W) \,. \tag{15}$$

If the initial rotation is subcritical, $W_o < 1$, then the actual spindown age is shorter by a time $\Delta t_{\rm s} = \tau_{\rm J} \ln W_o$.

As noted previously, the extra axes in Fig. 3 give the spindown time-scale $\tau_{\rm J}$ normalized by the value in a non-magnetized wind (i.e. by how much the magnetic braking enhances the stellar spindown) along the top, and the maximum spindown age $t_{\rm s,\,max}$ normalized by the spindown time (i.e. the number of spindown e-folds) along the right. For each of the individual magnetic OB stars, Columns 8 and 9 of Table 6 also list estimated values for, respectively, the spindown time $\tau_{\rm J}$ and the maximum spindown age $t_{\rm s,\,max}$ in Myr. Future studies can thereby compare $t_{\rm s,\,max}$ with other indicators of stellar age, for example from stellar evolution tracks or cluster association. To the extent that such independent age estimates are available, then within the limits of the stated assumptions of constancy in R_*, f and $\dot{J}$, a comparison with this spindown age could be used to estimate an initial rotation fraction W_o.

More immediately, note that among the full magnetic sample, many of the most slowly rotating stars are O-type stars. The high luminosities of these stars drive strong stellar winds that lead to a rapid angular momentum mass loss and thus very short spindown times. These characteristics help to explain their very slow rotation relative to many of the B-type targets. Except for Plaskett's star (ID 6), which has likely been spun up by binary interaction and show CM-type emission at high velocity (Grunhut et al. 2012b), all the rapidly rotating stars near the top of Fig. 3 are lower luminosity B-type stars with weaker winds; for magnetic B-type stars, the spindown time is thus generally longer than for the magnetic O-type stars, typically several Myr.

Indeed, extended photometric monitoring of the strongly magnetic B-type star σ Ori E (ID 31) has provided a direct measurement of the change in rotation period, yielding a spindown time of 1.34 Myr (Townsend et al. 2010, 2012). This is remarkably close to the spindown time of 1.4 Myr *predicted* previously by the scaling developed from MHD simulations (ud-Doula et al. 2009), but such very close agreement was likely fortuitous given the uncertainties in the mass-loss rate and stellar parameters. Indeed, the Vink et al. (2000, 2001) mass-loss rate we use here is roughly a factor of 10 smaller than the CAK mass-loss rate assumed by ud-Doula et al. (2009), leading to a factor of $\sim\sqrt{10}$ longer estimate for the spindown time, 4.6 Myr. This emphasises that our listed values spindown time and age are only estimates accurate to within a factor of 3 or so.[7]

4 Hα AS A MAGNETOSPHERIC PROXY

We now explore how magnetospheric Hα emission characteristics correlate with their position in the magnetic confinement–rotation diagram.

4.1 Identification of Hα magnetospheric emission

In Table 6, Column 11 indicates the emission (em) versus absorption (abs) nature of the Hα line, and, if enough observations ($\gtrsim$5) are available, whether the profile is stable (stab) or variable (var). We flag Herbig Be stars (HeBe) because of the difficulty in disentangling magnetospheric emission from the emission produced by the accretion discs characteristic to this class of pre-main-sequence stars. Similarly in the case of spectroscopic binaries, slowly pulsating B-stars and β Cep stars (indicated in Column 3), variation

[7] A change of period has also been measured for HD 37776 (ID 34; Mikulášek et al. 2011) with a spindown time-scale of 0.37 Myr, comparable to our $\tau_{\rm J}$ of 0.68 Myr. However, as discussed by ud-Doula et al. (2009), the complex field geometry of HD 37776 (Kochukhov et al. 2011) will have a potentially strong impact on the angular momentum evolution of this star.

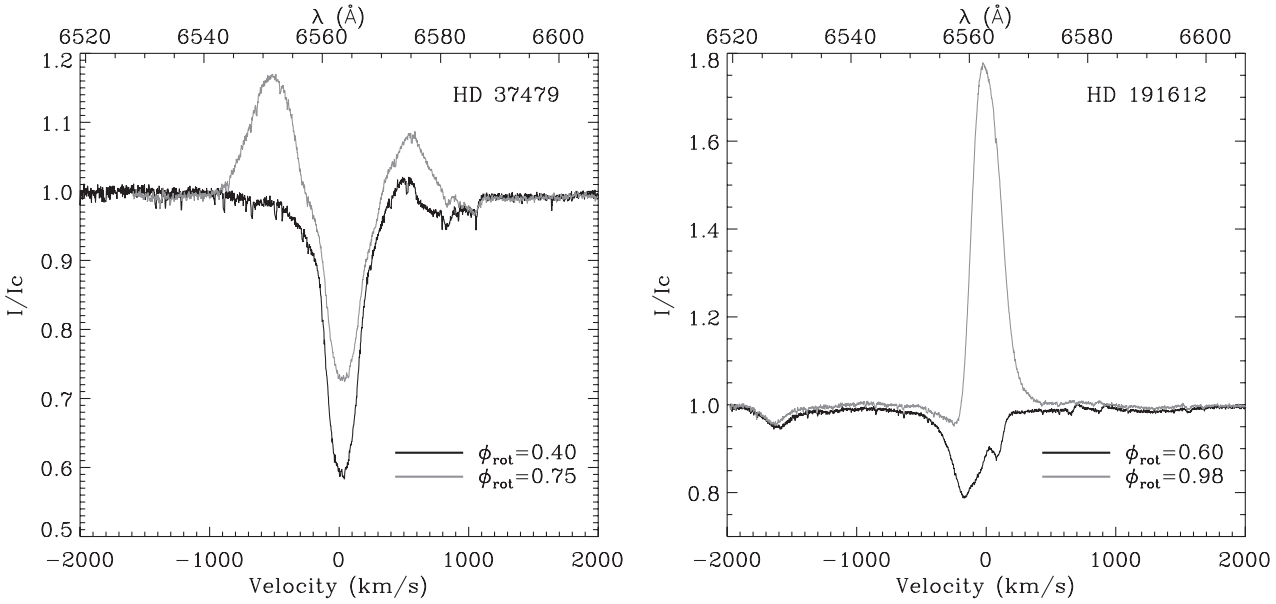

Figure 6. Example of Hα line profiles, from MiMeS observations, for a CM (left, σ Ori E, ID 31) and a DM (right, HD 191612, ID 4) and minimum (black) and maximum (grey) emission. Note how the extended emission wings are located at large velocities (outside $v \sin i$) for the CM, whereas the central emission is localized in a narrow range of velocities (inside $v \sin i$) in the line core for the DM.

in the absorption line profile may have non-magnetic origins, but emission can generally be attributed to a magnetosphere.

This emission can have various distinguishing characteristics: (1) a central absorption core with broad emission wings that extend well beyond the photospheric $v \sin i$ (Fig. 6, left); (2) strong, narrow emission that overwhelms the photospheric absorption profile (Fig. 6, right, grey profile); (3) weak overlying emission that only partially fills the underlying absorption (Fig. 6, right, black profile).

For type (3), there can be confusion with the line-filling effect of a non-magnetised stellar wind; a clear identification requires monitoring for rotational modulation.[8] For types (1) and (2), a single observation can suffice to identify a magnetospheric origin.

For type (1) the extended emission wings suggest plasma held in extended rigid-body rotation around the star, presumably by the stellar magnetic field. These correspond to CM, as described by Townsend & Owocki (2005). Multiple occurrences of this type of emission can be found in Bohlender & Monin (2011), Oksala et al. (2012), Grunhut et al. (2012b), as well as the references listed in Table 2.

For type (2), the narrow central emission suggests that the trapped plasma is kept at low velocities, without much broadening from rotation or from a high-speed outflow like in a non-magnetic stellar wind (Sundqvist et al. 2012). These correspond to dynamical magnetospheres (DM). Examples of such emission can be found in Howarth et al. (2007), Grunhut et al. (2012c), Wade et al. (2012a), as well as the references listed in Table 2.

4.2 Hα emission in the classification diagram

Fig. 7 (left) again plots stars in the confinement–rotation diagram, with symbols now coloured to mark the presence (dark pink) or absence (light purple) of magnetospheric Hα emission. Herbig stars are omitted here because of their intrinsic emission not associated with magnetic fields. While stars with and without emission are found throughout the diagram, note that in the DM region with $R_A < R_K$, all the emission occurs (with just one exception, HD 156424; ID 36) in O-type stars, for which the large luminosity suggests the wind feeding of the DM is strong enough to build up sufficient density for emission within the dynamical infall time-scale. The same strong wind mass loss that feeds the DM emission means that they have relatively strong angular momentum loss that spins down the stars to their observed slow rotation rates near the bottom of the confinement–rotation diagram.

Conversely, in the CM region with $R_A > R_K$, the emission (again with one exception, Plaskett's star, ID 6) occurs in B-type stars, for which the lower luminosity and wind feeding require the longer retention time-scale of a CM to build up sufficient density for emission. In fact, all the non-emitting stars in this region are also B-type, indicating that a CM is a necessary but not sufficient condition for emission for such low-luminosity stars with relatively weak wind mass loss. Most of the B-type stars with emission are in the extreme upper right of the diagram, with both strong confinement and rapid rotation. Their wide separation from the $R_A = R_K$ line implies a large radial extent for their CM.

Overall, this link between Hα emission and location in the magnetic confinement–rotation diagram provides a useful categorization that connects the rotation, mass loss and circumstellar emission properties of massive-star magnetospheres.

4.3 Magnetospheric versus stellar properties

To explore further this categorization, Fig. 8 plots (again for all the non-Herbig stars) the log of the ratio R_A/R_K (Column 10 of Table 6) versus stellar effective temperature T_{eff} (left) or bolometric luminosity $L_\star$ (right), with symbols again marking spectral type, coloured for the presence (dark pink) or absence (light purple) of magnetospheric Hα emission (Fig. 9 provides a finding chart). The single upward arrows indicate stars that could be shifted upwards due to either a higher polar field than the minimum inferred from

[8] Modulated variations in the core of absorption lines could also have other origins, for example changes in the photospheric structure due to large helium abundance inhomogeneities on the surface of chemically peculiar stars (e.g. a Cen; ID 63, Bohlender et al. 2010).

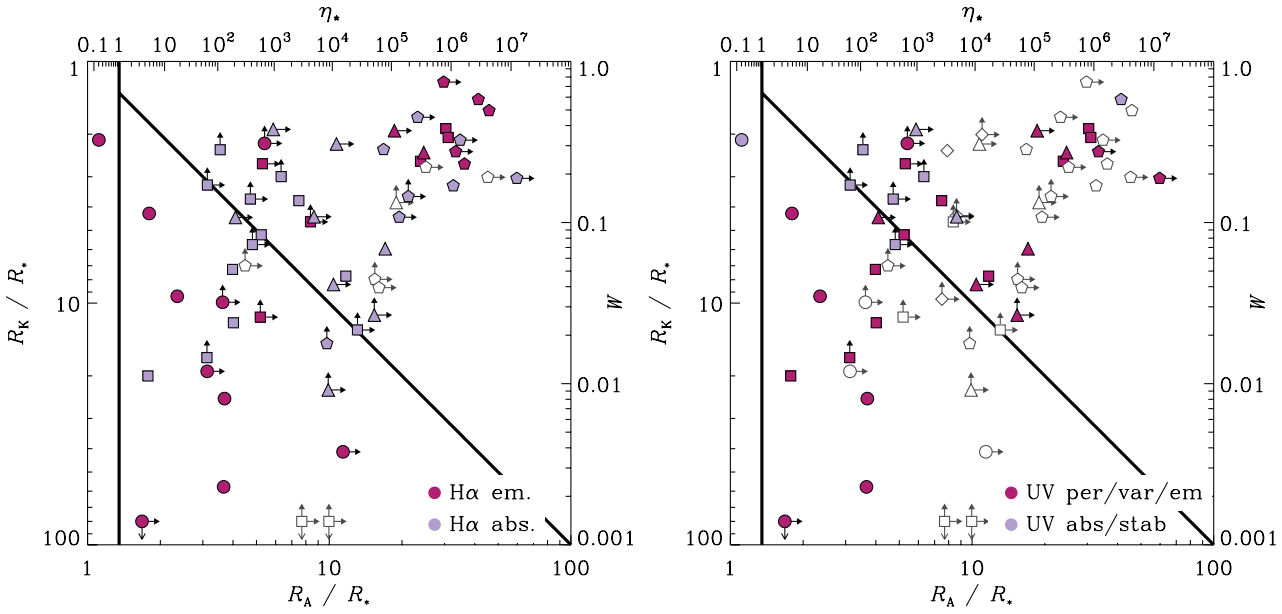

Figure 7. Location of magnetic massive stars in the magnetic confinement–rotation diagram (see Fig. 3). The symbols are coloured to mark the presence (dark pink) or absence (light purple) of a magnetospheric signature in Hα emission (left) and UV resonance line (right), as described in Table 6, and in Sections 4.1 and 5.1, respectively. The symbols are empty when no information is available.

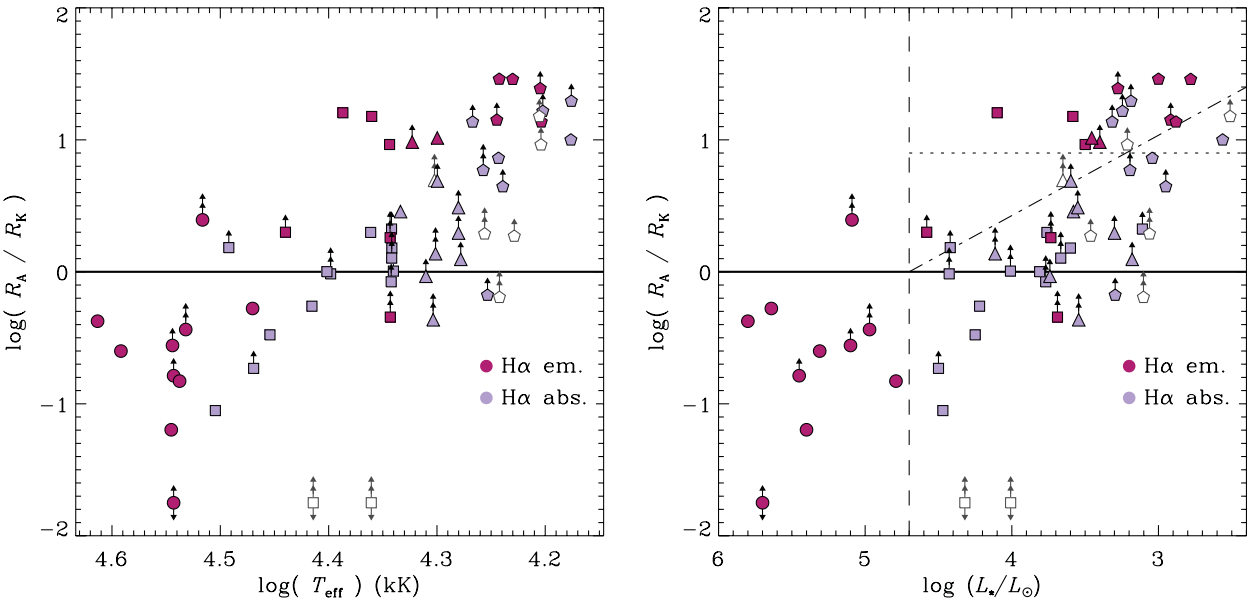

Figure 8. Location of magnetic massive stars in a log –log plot of R_A/R_K versus the effective temperature (left) and the luminosity (right). The symbols are coloured to mark the presence (dark pink) or absence (light purple) of magnetospheric Hα emission, as described in Table 6 and Section 4.1. The symbols are empty when no Hα information is available. Single arrows indicate a limit on either R_A or R_K, whereas double arrows mark stars for which both R_A and R_K are limits. In the right-hand diagram, the vertical dashed line represents the luminosity transition between O-type and B-type main-sequence stars. The horizontal dotted line and the diagonal dot–dashed line are illustrative division of the CM domain according to potential mass leakage mechanisms (see discussion in Section 4.3).

the available longitudinal field measurements (increasing R_A), or a higher rotation rate than the minimum inferred from the measured $v \sin i$ (decreasing R_K); the *double* upward arrows indicate stars for which *both* limits are at play.

The solid horizontal line at $R_A = R_K$ separates the domains for DM at the bottom from CM at the top, with the distance above the line characterizing the radial extent for the centrifugal support. Each plot again shows that Hα emission occurs both in O-type stars to the left, and in B-type stars to the (mostly upper) right; but the demarcation is particularly distinct in the plot versus bolometric luminosity.

In that plot, the vertical dashed line corresponds roughly to the main-sequence transition from O- to B-type stars (Martins et al. 2005). The O-type stars to the left all have clear Balmer emission. Except for Plaskett's star (ID 6), which has likely been spun up by binary interaction, they also are all relatively slow rotators with $R_A < R_K$ (DM). Their high luminosity means they have strong stellar winds, implying both a rapid stellar spindown and a sufficient

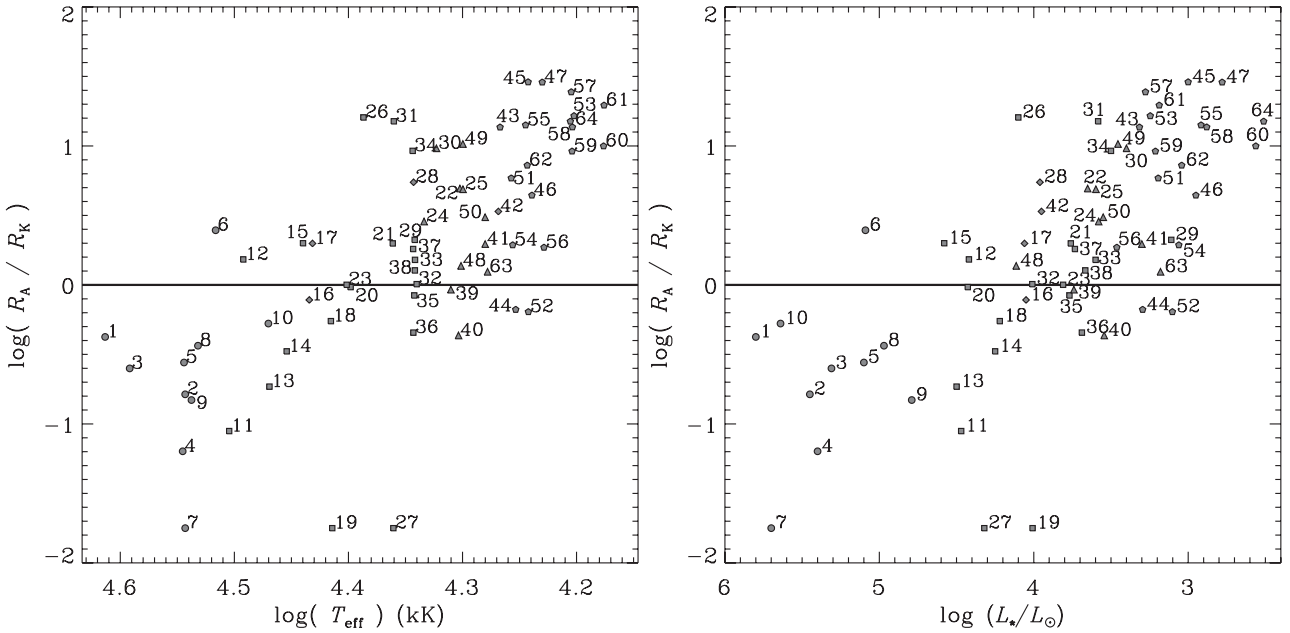

Figure 9. Finding charts for the location of magnetic massive stars in a log–log plot of R_A/R_K versus the effective temperature (left) and the luminosity (right). The label numbers correspond to the ID in Column 1 of Table 1.

magnetospheric density to give line emission in the short residence time for a DM.

For B-type stars to the right of this vertical line, emission is most common in the most rapidly rotating stars above the horizontal dotted line at $\log(R_A/R_K) = 0.9$. The four stars above this line without detected emission are all relatively late-type stars, with low luminosity and so likely a very low wind mass-loss rate to feed the expected CM. The three stars *below* this line *with* detected emission have arrows indicating they could shift upwards, with the two lower luminosity stars (HD 156424 and HD 156324; ID 36, 37) having double arrows indicating potentially significant revision in both field strength and rotation rate. Indeed, although the current MiMeS observations do not allow for clear determination of a rotation period, in both cases the nightly variation of longitudinal field measurements points towards periods of the order of a day. These stars are prime candidates for follow up observations.

The third, relatively high-luminosity B-type star (ξ^1 CMa; ID 15) has a well-determined period and Kepler radius, but still has a single arrow from the limited polar field estimate. Its current position – just above the horizontal solid line, and just to the right of the vertical dashed line – makes it a particularly interesting test case for magnetospheric models, very near the transition from DM to CM, and from O-type stars to B-type stars mass loss.

Indeed, if the CM/B-type star occurrence of Hα emission depends on a *combination* of the radial extent of the CM (set by R_A/R_K and thus the vertical position in Fig. 8) and on the mass-loss rate feeding the CM (set by the luminosity and thus the horizontal position in Fig. 8), then we can identify a possible further division along the illustrative *diagonal* dot–dashed line in Fig. 8. It would thus be of particular interest to clarify the position, and the emission properties, of stars with current placements near this illustrative diagonal line.

Establishing empirically whether the onset of emission is better delineated by the horizontal dotted line or the diagonal dot–dashed line has potentially important implications for our theoretical understanding of the magnetospheric mass budget. The former would indicate that the CM mass depends mainly on the *capacity* for the magnetic field to confine centrifugally supported material, which eventually fills to a fixed level even if at the slow rate from a weak wind. The latter would indicate a competing *leakage* from the CM that decreases with distance above the $R_A = R_K$ line. To build up sufficient density for emission, stars near the $R_A = R_K$ line with high leakage require a high mass-loss rate and thus high luminosity, representing the left end of the diagonal; stars further above the line with lower leakage can fill their CM even with the weaker wind from a lower luminosity, representing the upper right end of the diagonal.

As a shorthand, we might identify these as the 'capacity' versus 'leakage' models for determining the onset of CM emission. Hopefully, the classification and physical arguments here will motivate a concentrated observational programme to clarify the position, and the emission properties, of the key stars for establishing this discrimination.

5 OTHER MAGNETOSPHERIC PROXIES

5.1 Ultraviolet variability

In hot, massive stars, strong UV resonance lines like C IV λλ 1548, 1550, Si IV λλ 1393, 1403 and N V λλ 1239, 1243 are typically used as diagnostics of the stellar wind. In O-type stars with dense winds, the line profiles generally exhibit a characteristic P-Cygni profile showing red-side emission and blue-side absorption, with the blue edge of the latter marking the wind terminal speed. In B-type stars with weaker winds, the emission is weak or absent, and the blue edge of the shallower absorption may not extend to the terminal speed. Both types can exhibit intrinsic variability, but this is most common, distinctive and well-studied in O-type stars, for which it is generally characterized by discrete absorption components (DACs) that start near line-centre and slowly propagate across the blue absorption trough (e.g. Howarth & Prinja 1989; Kaper et al. 1996). These are likely representations of spiral-shaped density compressions,

referred to as Corotating Interacting Regions (CIRs; Mullan 1986), caused by faster moving streams overtaking slower moving streams, where the interacting interface between the two is shocked. The projected velocity in the line of sight progresses because of the stellar rotation, rather than because of the outflow itself (Cranmer & Owocki 1996).

In magnetic OB stars these UV lines can be strongly affected by changes in velocity, density, and/or ionization balance. Indeed, it was recognized early on that *periodic* variations of the resonance lines could point towards the presence of a rotating magnetosphere (e.g. Shore & Brown 1990; Henrichs et al. 1993; Walborn & Nichols 1994). In contrast, the appearance of DACs is often found to be cyclical but never strictly periodic. Moreover, unlike the blueward-propagating DACs, in magnetic OB stars UV line variation occurs nearly coherently and synchronously over the full velocity range of the profile (e.g. Henrichs et al. 2012; Marcolino et al. 2012). Thus, even in those stars without sufficient monitoring to clearly establish a period, one could use the morphological character of variations between two or more observations to flag the likely presence of a strong field (e.g. Henrichs et al. 2012).

In B-type stars, UV profiles show only shallow (if any) blueward wind absorption and weak or absent redward emission. The appearance of strong redward emission along with filling in of the absorption (see fig. 5 of Shore & Brown 1990) can likewise be used to flag the likely presence of a magnetosphere, even without multiple observations to show variability.

Column 12 of Table 6 gives a summary characterization of UV resonance lines for the full sample of magnetic stars. The listed UV signatures of a field include periodicity (per), profile variability with morphology similar to periodic stars (var) and, for B-type stars, distinct redward emission with missing blueward absorption (em). Stars lacking a clear UV magnetic signature are those with only pure absorption (abs), and those with five or more observations showing stable absorption (stab abs). When available, these characterisations are from the literature, as summarized in Table 2, and otherwise are based on visual inspection of IUE archive spectra.

In analogy with the organization of Hα signatures shown in the left-hand panel of Fig. 7, the right-hand panel again plots stars in the magnetic confinement–rotation diagram, but now with stars showing one or more UV signatures for a field marked in dark pink, and those with absorption profiles consistent with lack of a field marked in light purple. Stars without UV observations (or IUE spectra with too low signal-to-noise ratio) have empty symbols.

Note that, in contrast to Hα emission, such UV magnetic signatures occur throughout the diagram, and for all spectral types. In particular, B-type stars with weak winds show a UV magnetic signature even in the slow-rotation, DM region, for which B-type star Hα emission is not seen. Thus UV variation seems to be a widespread phenomenon among magnetic OB stars, as long as some confinement is present, and therefore represents a relatively robust proxy of magnetism. In fact, a number of magnetic OB stars had been first identified as peculiar UV stars (e.g. Henrichs et al. 1993, 2012; Neiner et al. 2003b).

The few stars without signs of UV variability cluster at lower R_A, but many other stars show UV field signatures in the same region of the diagram. As suggested by Shore & Brown (1990) for some of the Bp stars, the exact behaviour of the variability might be closely tied with the geometry of the magnetic field with respect to the observer. Thus detailed modelling of the UV line profiles for magnetic OB stars may help constrain the geometry of the magnetospheres and clarify the velocity and ionization structure of the trapped material.

Indeed, UV resonance-line synthesis from MHD models shows clear P-Cygni absorption troughs that are modulated on the rotation phase. For relatively strong lines, such troughs are actually deeper when viewing the magnetosphere pole-on than equator-on (ud-Doula 2008). This somewhat counterintuitive effect occurs because the overdense material around the magnetic equator is characterized by very low velocities, whereas the outflow above the pole more closely resembles that of a normal, non-magnetic wind. Thus the absorption column above the pole covers a much wider velocity range, leading to wider and deeper troughs.

However, further calculations also suggest that the phase variability of such UV lines is quite sensitive to the actual strength of the line itself, and so may depend critically on the stellar mass-loss rate as well as on the magnetospheric ionization state (Sundqvist et al., in preparation). The strong UV lines in HD 108 (ID 7) indeed seem to display the characteristic variability described above (Marcolino et al. 2012), but those in θ^1 Ori C (ID 3) show effectively the opposite behaviour (ud-Doula 2008). Thus further modelling work is still needed to fully understand how magnetic fields affect the formation of UV lines of OB stars.

5.2 X-rays

Massive stars are generally X-ray bright due to the intrinsic instability of the line-driving mechanism for radiative stellar winds (Feldmeier, Puls & Pauldrach 1997; Runacres & Owocki 2002; Dessart & Owocki 2003), with a well-known canonical value for early OB star X-ray luminosity, L_X, of $\sim 10^{-7.2} L_\star$ (Berghoefer et al. 1997; Gagné et al. 2011; Nazé et al. 2011). The magnetically channelled wind shocks (MCWS scenario) associated with magnetic massive stars should also generate even stronger and harder X-ray emission by the radiative cooling of the shock heated plasma in the magnetosphere (Babel & Montmerle 1997a). For example, the X-rays from the O-type star θ^1 Ori C (ID 3) are more luminous and harder than in typical O-type stars, and modulated by the rotational period. Gagné et al. (2005) used 2D MHD simulations, including an explicit energy equation, to track the shock heated material and its radiative cooling, and were able to reproduce the X-ray properties of θ^1 Ori C, including the star's elevated X-ray luminosity, high plasma temperature, rotational modulation and narrow spectral lines. Therefore, it seems at first glance that luminous, hard and variable X-ray emission could be a proxy for magnetism in massive stars.

However, these characteristics are not always present in magnetic massive stars. For example, the B-type star τ Sco (ID 11) is X-ray luminous and indeed displays a hard X-ray spectrum (Mewe et al. 2003), but it does not show evidence of rotational modulation (Ignace et al. 2010). The B-type star NU Ori (ID 12) does not show any significant variability over the duration of a $\sim$10 d *Chandra* observation (Stelzer et al. 2005), and has a soft spectrum. Another prototypical magnetic O-type star is the Of?p star HD 191612 (ID 4) which is quite luminous, but has a rather soft spectrum (Nazé et al. 2010). Oskinova et al. (2011) recently examined a small subset of magnetic B stars and noted that they too have diverse X-ray properties, including a few that are not X-ray overluminous at all.

We present here a first attempt to cast the X-ray characteristics of our large sample of magnetic OB stars as a function of their magnetospheric properties, focusing on just the X-ray luminosity. We perform a review of the literature to extract X-ray fluxes for the stars in our sample. Where possible, we use X-ray fluxes derived from pointed observations by modern X-ray observatories (*Chandra* and *XMM*) and reported in papers that carefully model the emission properties, correcting for interstellar absorption. A large majority

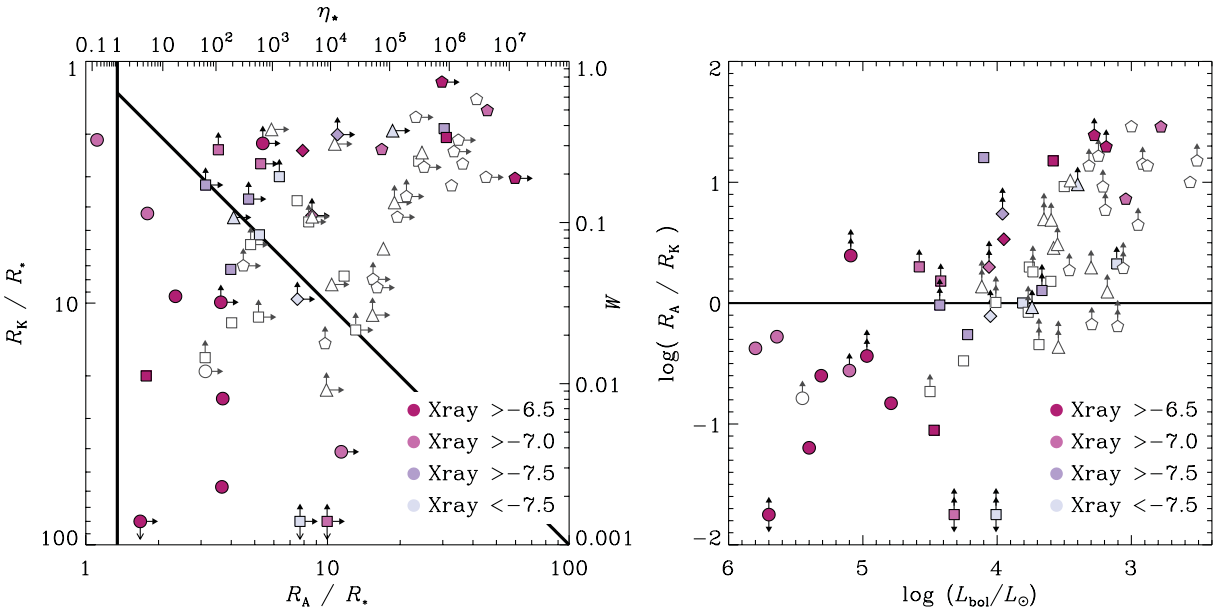

Figure 10. Location of magnetic massive stars in the magnetic confinement–rotation diagram (left) and in a log–log plot of R_A/R_K versus the luminosity (right). The stars are colour-coded according to their X-ray luminosity with respect to their bolometric luminosity [$\log(L_X/L_\star)$] in bins of 0.5 dex. The dark pink shades represent stars with $\log(L_X/L_\star)$ greater than the canonical value of −7 for early OB stars and the light purple shades for stars below this value. The symbols are empty when no X-ray information is available.

of the O-type and very early B-type stars in our sample fall into this category. For these stars, differences in the instrument bandpasses and uncertainties associated with the multi-temperature emission modelling and the interstellar medium (ISM) correction should lead to errors in the reported X-ray fluxes of less than a factor of 2. We correct all of the literature X-ray luminosities for the distances adopted by the authors of each paper to derive an X-ray flux, and then recompute the X-ray luminosity using the distances we adopt for each star, which of course are consistent with the distances we use for the bolometric luminosity determinations. We then compute the X-ray efficiency ratio $\log(L_X/L_\star)$ (Column 13 of Table 6), so that even if better distance determinations are made for some of these objects in the future, their $\log(L_X/L_\star)$ values will not have to be adjusted.

For many of the later B-type stars, no X-ray measurements exist, and for others only survey data, primarily from *ROSAT*, exist. The X-ray fluxes derived for these stars are more uncertain, primarily because of the lack of detailed spectral modelling and in some cases the lack of detailed ISM absorption corrections. Additionally, the bandpass of *ROSAT* is softer than that of either *XMM* or *Chandra*, further skewing comparisons between the derived X-ray luminosities. There are similar considerations for the small number of B-type stars for which only *EINSTEIN* measurements exist (Grillo et al. 1992). A more conservative estimate of the $\log(L_X/L_\star)$ uncertainties for these stars is required, with the overall error being probably up to 0.5 dex. Another factor potentially affecting our X-ray luminosity determinations is the contribution from unresolved binary companions (e.g. Petit et al. 2012). This phenomenon is more likely to be important for later B-type stars, observed with X-ray telescopes with poorer spatial resolution, and with lower intrinsic X-ray luminosities such that low-mass pre main sequence companions could account for much of the observed X-ray emission for a given star. However, it is unlikely that all the X-ray bright magnetic B-type stars are affected by binarity. For example, Gagné et al. (2011) have shown that the pre-main-sequence population of the Carina Complex cannot explain all the X-ray emission of B-type stars and that some of them must be intrinsically X-ray bright.

In Fig. 10 (left), we plot the stars in the R_A–R_K plane with a colour coding representing the X-ray efficiency ratio in bins of 0.5 dex ([>−6.5], [−6.5,−7.0], [−7.0,−7.5] and [<−7.5]). The dark pink shades are for stars with X-ray efficiency greater than the canonical value of $\log(L_X/L_\star) = -7.0$ for O-type stars. All the O-type stars show some level of overluminosity [$\log(L_X/L_\star) > -6.7$]. Some of the B-type stars also show overluminosity. Most of them are located in the upper part of the CM region, although a few overluminous, very early B-type stars are located in the DM region. The right-hand panel of Fig. 10 presents a logarithmic plot of R_A/R_K versus the bolometric luminosity. One can see that enhanced X-ray emission generally occurs for the most luminous magnetic OB stars. The B-type stars with intermediate luminosities seem to have X-ray emission typical for their spectral type, although it has been shown that the L_X–$L_\star$ relation breaks down at spectral type B2 and that the typical L_X is $10^{-8}L_\star$ or lower for later spectral types (Cohen et al. 1997), implying that *any* mid B-type star in one of the three highest $\log(L_X/L_\star)$ bins is overluminous for its spectral subtype. Finally, some low-luminosity stars with large R_A/R_K (extended CM) show enhanced X-ray emission.

A potential explanation for the X-ray emission enhancement in CM is the centrifugal acceleration for fast rotators, which contributes by propelling the confined material up the magnetic loop leading to stronger shocks than what could be achieved by radiative acceleration alone like in a DM. However, Rigid-Field Hydrodynamical (RFHD; Townsend et al. 2007) simulations predict that the overall X-ray flux of stars in the CM region is also quite sensitive to the mass-loss rate. The distribution in temperature of the differential emission measure (DEM) is governed by both the pre-shock and post-shock characteristics of the magnetosphere. Both of these are affected by the wind properties, with the post-shock cooling length being longer for lower-density wind flows, leading to softer and weaker emission (Hill et al. 2011).

Therefore, a complete survey of the X-ray properties of the magnetic OB stars would be highly desirable as X-ray emission could provide a different perspective on the structure and dynamics of magnetospheres, and the shock physics occurring in both DMs and CMs. Future studies should include a consistent and uniform analysis of (1) X-ray plasma temperature distributions and (2) time-variability. Although a re-analysis of all the available X-ray observations is beyond the scope of the current paper, the work presented here can be used as a starting point for identifying interesting stars for which X-ray data already exist, as well as identifying stars with interesting positions in the magnetic confinement–rotation diagram for which acquiring X-ray observations should be a priority. Another key development for understanding the trends identified above in the X-ray emission of magnetic massive stars would be more accurate and secure wind mass-loss rates for the B-type stars.

6 CONCLUSIONS

The MiMeS project aims to study the scope and impact of stellar magnetism in massive stars using high-resolution and high signal-to-noise ratio spectropolarimetric observations from Large Programme time allocations. Within this context, the present study had two main goals: (1) to compile an exhaustive and well-documented list of confirmed magnetic, hot OB stars that are directly detected through the Zeeman effect, and (2) to organize the stars in a way that accounts for both the strength of magnetic confinement of the stellar wind (through η_* or R_A) and the dynamical role of stellar rotation (through W or R_K). Key results are as follows.

(i) We have provided a compilation of relevant stellar parameters for our magnetic sample. We used the luminosity, mass and radius obtained from modern spectral modelling from the literature, when available; otherwise, these were derived from a classical BC approach, and from SED fitting with the code CHORIZOS when a complete set of photometry was available. We have also compiled rotational periods and dipolar field strengths, as well as binarity and pulsation status.

(ii) Using these parameters, we have placed the full sample of magnetic stars in a classification plane, the magnetic confinement–rotation diagram, characterizing stellar rotation (as R_K or W) versus wind magnetic confinement (as R_A or η_*).

(iii) We identified key domains within the magnetic rotation-confinement diagram, representing weakly magnetized winds with $\eta_* \lesssim 1$, or DMs (with $R_* < R_A < R_K$) versus CMs (with $R_* < R_K < R_A$).

(iv) We have associated Hα line emission characteristics with position in the confinement–rotation diagram. Slowly rotating O-type stars show DM magnetospheric emission in contrast to B-type stars which generally only show CM magnetospheric emission.

(v) In a plane plotting the ratio R_A/R_K versus stellar luminosity, we found a clear separation between O-type star DM emission and B-type stars for which appearance of CM emission requires higher R_A/R_K for lower luminosity stars. This suggests that the CM leakage mechanism may depend on the degree of magnetic confinement.

(vi) We have also associated other magnetospheric proxies with position in the confinement–rotation diagram. UV resonance line variation occurs in all magnetosphere regimes and for stars of all temperatures; although detailed modelling will be needed in the future, UV spectroscopy seems an excellent proxy for identifying new magnetic OB stars. The earliest magnetic OB stars generally show X-ray overluminosity, as do the low-luminosity B-type stars with large CM volumes (high R_A/R_K).

(vii) We have calculated magnetic spindown time-scales (τ_J) and inferred spindown ages (t_s) for each star in our sample. O-type stars with strong winds have short spindown time-scales and so mostly are slow rotators located in the DM region; B-type stars with weaker winds have longer spindown time-scales, and thus extend well into the CM regime with rapid rotation.

(viii) Finally, we have identified stars which will be prime candidates for follow-up studies (with either unknown periods or only dipole field strength lower limits) that would lead to a more accurate placement on the confinement–rotation diagram, hence providing more clues to the answers of some of the questions raised in this paper.

ACKNOWLEDGMENTS

VP acknowledges support from Fonds québécois de la recherche sur la nature et les technologies. SOP and JOS acknowledge support from NASA grant ATP NNX11AC40G. GAW acknowledges support from the Natural Science and Engineering Research Council of Canada (NSERC) Discovery Grant programme. MEO acknowledges financial support from GA ČR under grant number 209/11/1198. The Astronomical Institute Ondřejov is supported by the project RVO:67985815. EA thanks the Programme National de Physique Stellaire (PNPS) for its support. RHDT and Au-D acknowledge support from NASA grant NNX12AC72G. This research has made use of the SIMBAD data base, operated at CDS, Strasbourg, France, and the Canadian Astronomy Data Centre operated by the National Research Council of Canada. The authors would like to thank the MiMeS observing team for their efforts and the anonymous referee for his comments.

REFERENCES

Abt H. A., Wang R., Cardona O., 1991, ApJ, 367, 155
Alecian E. et al., 2008a, MNRAS, 385, 391
Alecian E. et al., 2008b, A&A, 481, L99
Alecian E. et al., 2011, A&A, 536, L6
Ausseloos M., Aerts C., Lefever K., Davis J., Harmanec P., 2006, A&A, 455, 259
Babcock H. W., 1947, ApJ, 105, 105
Babel J., Montmerle T., 1997a, ApJ, 485, L29
Babel J., Montmerle T., 1997b, A&A, 323, 121
Bagnulo S., Landstreet J. D., Mason E., Andretta V., Silaj J., Wade G. A., 2006, A&A, 450, 777
Bagnulo S., Landstreet J. D., Fossati L., Kochukhov O., 2012, A&A, 538, A129
Berghoefer T. W., Schmitt J. H. M. M., Danner R., Cassinelli J. P., 1997, A&A, 322, 167
Bohlender D. A., 1989, ApJ, 346, 459
Bohlender D. A., Landstreet J. D., 1990, ApJ, 358, 274
Bohlender D. A., Monin D., 2011, AJ, 141, 169
Bohlender D. A., Landstreet J. D., Brown D. N., Thompson I. B., 1987, ApJ, 323, 325
Bohlender D. A., Rice J. B., Hechler P., 2010, A&A, 520, A44
Bolton C. T., Harmanec P., Lyons R. W., Odell A. P., Pyper D. M., 1998, A&A, 337, 183
Borra E. F., 1981, ApJ, 249, L39
Borra E. F., Landstreet J. D., 1980, ApJS, 42, 421
Bouret J.-C., Donati J.-F., Martins F., Escolano C., Marcolino W., Lanz T., Howarth I. D., 2008, MNRAS, 389, 75
Bouret J.-C., Hillier D. J., Lanz T., Fullerton A. W., 2012, A&A, 544, A67
Briquet M., Aerts C., De Cat P., 2001, A&A, 366, 121
Briquet M., Aerts C., Lüftinger T., De Cat P., Piskunov N. E., Scuflaire R., 2004, A&A, 413, 273

Briquet M., Hubrig S., Schöller M., De Cat P., 2007, Astron. Nachr., 328, 41
Brott I. et al., 2011, A&A, 530, A115
Bychkov V. D., Bychkova L. V., Madej J., 2005, A&A, 430, 1143
Castor J. I., Abbott D. C., Klein R. I., 1975, ApJ, 195, 157 (CAK)
Catanzaro G., 2008, MNRAS, 387, 759
Chauville J., Zorec J., Ballereau D., Morrell N., Cidale L., Garcia A., 2001, A&A, 378, 861
Cidale L. S., Arias M. L., Torres A. F., Zorec J., Frémat Y., Cruzado A., 2007, A&A, 468, 263
Claret A., 2004, A&A, 424, 919
Cohen D. H., Cassinelli J. P., Macfarlane J. J., 1997, ApJ, 487, 867
Collins G. W. II, Harrington J. P., 1966, ApJ, 146, 152
Cranmer S. R., Owocki S. P., 1996, ApJ, 462, 469
de Jager C., Nieuwenhuijzen H., 1987, A&A, 177, 217
Dessart L., Owocki S. P., 2003, A&A, 406, L1
Donati J., Landstreet J. D., 2009, ARA&A, 47, 333
Donati J.-F., Wade G. A., Babel J., Henrichs H. F., de Jong J. A., Harries T. J., 2001, MNRAS, 326, 1265
Donati J.-F., Babel J., Harries T. J., Howarth I. D., Petit P., Semel M., 2002, MNRAS, 333, 55
Donati J.-F., Howarth I. D., Bouret J.-C., Petit P., Catala C., Landstreet J., 2006a, MNRAS, 365, L6
Donati J.-F. et al., 2006b, MNRAS, 370, 629
Drake S. A., Linsky J. L., Schmitt J. H. M. M., Rosso C., 1994, ApJ, 420, 387
Favata F., Neiner C., Testa P., Hussain G., Sanz-Forcada J., 2009, A&A, 495, 217
Feldmeier A., Puls J., Pauldrach A. W. A., 1997, A&A, 322, 878
Fourtune-Ravard C., Wade G. A., Marcolino W. L. F., Shultz M., Grunhut J. H., Henrichs H. F., Henrichs 2011, in Neiner C., Wade G., Meynet G., Peters G., eds, IAU Symp. Vol. 272. Active OB Stars: Structure, Evolution, MassLoss, and Critical Limits. Cambridge Univ. Press, Cambridge, p. 180
Gagné M., Oksala M. E., Cohen D. H., Tonnesen S. K., ud-Doula A., Owocki S. P., Townsend R. H. D., MacFarlane J. J., 2005, ApJ, 628, 986
Gagné M. et al., 2011, ApJS, 194, 5
Gayley K. G., 1995, ApJ, 454, 410
Glagolevskij Y. V., Leushin V. V., Chountonov G. A., 2007, Astrophys. Bull., 62, 319
Grillo F., Sciortino S., Micela G., Vaiana G. S., Harnden F. R. Jr, 1992, ApJS, 81, 795
Grunhut J. H. et al., 2009, MNRAS, 400, L94
Grunhut J. H. et al., 2012a, MNRAS, 419, 1610
Grunhut J. H. et al., 2012b, MNRAS, in press (arXiv:1209.6326)
Grunhut J. H. et al., 2012c, MNRAS, 426, 2208
Guarcello M. G., Caramazza M., Micela G., Sciortino S., Drake J. J., Prisinzano L., 2012, ApJ, 753, 117
Hamaguchi K., Yamauchi S., Koyama K., 2005, ApJ, 618, 360
Hauck B., Mermilliod M., 1998, A&AS, 129, 431
Henrichs H. F., Bauer F., Hill G. M., Kaper L., Nichols-Bohlin J. S., Veen P. M., 1993, in Nemec J. M., Matthews J. M., eds, IAU Colloq. 139: New Perspectives on Stellar Pulsation and Pulsating Variable Stars. Cambridge Univ. Press, Cambridge, p. 186
Henrichs H. F. et al., 2009, in Strassmeier K. G., Kosovichev A. G., Beckmann J., eds, IAU Symp. Vol. 259, Cosmic Magnetic Fields: from Planets, to Stars and Galaxies. Cambridge Univ. Press, Cambridge, p. 393
Henrichs H. F. et al., 2012, A&A, 545, 119
Hill N. R., Townsend R. H. D., Cohen D. H., Gagné M., 2011, in Neiner C., Wade G., Meynet G., Peters G., eds, IAU Symp. Vol. 272, Active OB Stars: Structure, Evolution, MassLoss, and Critical Limits. Cambridge Univ. Press, Cambridge, p. 194
Hillier D. J., Miller D. L., 1998, ApJ, 496, 407
Howarth I. D., Prinja R. K., 1989, ApJS, 69, 527
Howarth I. D., Walborn N. R., Lennon D. J., Puls J., 2007, MNRAS, 381, 433
Huang W., Gies D. R., 2006, ApJ, 648, 580
Hubrig S., Briquet M., Schöller M., De Cat P., Mathys G., Aerts C., 2006, MNRAS, 369, L61
Hubrig S., Briquet M., De Cat P., Schöller M., Morel T., Ilyin I., 2009, Astron. Nachr., 330, 317
Hummel C. A., White N. M., Elias N. M. II, Hajian A. R., Nordgren T. E., 2000, ApJ, 540, L91
Hunger K., Heber U., Groote D., 1989, A&A, 224, 57
Ignace R., Oskinova L. M., Jardine M., Cassinelli J. P., Cohen D. H., Donati J.-F., Townsend R. H. D., ud-Doula A., 2010, ApJ, 721, 1412
Kaper L., Henrichs H. F., Nichols J. S., Snoek L. C., Volten H., Zwarthoed G. A. A., 1996, A&AS, 116, 257
Kochukhov O., Lundin A., Romanyuk I., Kudryavtsev D., 2011, ApJ, 726, 24
Kraus S. et al., 2009, A&A, 497, 195
Kurucz R. L., 1979, ApJS, 40, 1
Lamers H. J. G. L. M., Snow T. P., Lindholm D. M., 1995, ApJ, 455, 269
Landstreet J. D., 1988, ApJ, 326, 967
Landstreet J. D., Borra E. F., 1978, ApJ, 224, L5
Landstreet J. D., Bagnulo S., Andretta V., Fossati L., Mason E., Silaj J., Wade G. A., 2007, A&A, 470, 685
Lanz T., Hubeny I., 2003, ApJS, 146, 417
Lanz T., Hubeny I., 2007, ApJS, 169, 83
Lee P., Obrien A., 1977, A&A, 60, 259
Lefever K., Puls J., Morel T., Aerts C., Decin L., Briquet M., 2010, A&A, 515, A74
Leone F., Manfre M., 1997, A&A, 320, 257
Leone F., Catalano F. A., Malaroda S., 1997, A&A, 325, 1125
Leone F., Bohlender D. A., Bolton C. T., Buemi C., Catanzaro G., Hill G. M., Stift M. J., 2010, MNRAS, 401, 2739
Linder N., Rauw G., Martins F., Sana H., De Becker M., Gosset E., 2008, A&A, 489, 713
Linsky J. L., Drake S. A., Bastian T. S., 1992, ApJ, 393, 341
Lutz T. E., Kelker D. H., 1973, PASP, 85, 573
Lyubimkov L. S., Rachkovskaya T. M., Rostopchin S. I., Lambert D. L., 2002, MNRAS, 333, 9
McSwain M. V., 2008, ApJ, 686, 1269
McSwain M. V., Huang W., Gies D. R., Grundstrom E. D., Townsend R. H. D., 2008, ApJ, 672, 590
Maíz-Apellániz J., 2001, AJ, 121, 2737
Maíz-Apellániz J., 2004, PASP, 116, 859
Maíz Apellániz J., 2005, in Turon C., O'Flaherty K. S., Perryman M. A. C., eds, ESA Special Publication Vol. 576, The Three-Dimensional Universe with *Gaia.* European Space Agency, p. 179
Maíz Apellániz J., 2012, in Guirado J. C., Lara L. M., Quilis V., Gorgas J., eds, Highlights of Spanish Astrophysics X. Spanish Astronomical Society, in press
Maíz Apellániz J., Alfaro E. J., Sota A., 2008, preprint (arXiv 0804.2553)
Marcolino W. L. F. et al., 2012, MNRAS, 422, 2314
Markova N., Puls J., 2008, A&A, 478, 823
Martins F., Plez B., 2006, A&A, 457, 637
Martins F., Schaerer D., Hillier D. J., 2005, A&A, 436, 1049
Martins F., Donati J., Marcolino W. L. F., Bouret J., Wade G. A., Escolano C., Howarth I. D., 2010, MNRAS, 407, 1423
Matthews J. M., Bohlender D. A., 1991, A&A, 243, 148
Mermilliod J. C., 2006, VizieR Online Data Catalog, 2168
Merrill P. W., Burwell C. G., 1943, ApJ, 98, 153
Mewe R., Raassen A. J. J., Cassinelli J. P., van der Hucht K. A., Miller N. A., Güdel M., 2003, A&A, 398, 203
Mikulášek Z., Krtička J., Henry G. W., Janík J., Zverko J., 2011, A&A, 534, L5
Mullan D. J., 1986, A&A, 165, 157
Najarro F., Hanson M. M., Puls J., 2011, A&A, 535, A32
Nazé Y., 2009, A&A, 506, 1055
Nazé Y., Rauw G., Pollock A. M. T., Walborn N. R., Howarth I. D., 2007, MNRAS, 375, 145
Nazé Y., Rauw G., Vreux J.-M., De Becker M., 2004, A&A, 417, 667

Nazé Y., ud-Doula A., Spano M., Rauw G., De Becker M., Walborn N. R., 2010, A&A, 520, A59
Nazé Y. et al., 2011, ApJS, 194, 7
Nazé Y., Bagnulo S., Petit V., Rivinius T., Wade G., Rauw G., Gagné M., 2012a, MNRAS, 423, 3413
Nazé Y., Zhekov S. A., Walborn N. R., 2012b, ApJ, 746, 142
Neiner C., Geers V. C., Henrichs H. F., Floquet M., Frémat Y., Hubert A., Preuss O., Wiersema K., 2003a, A&A, 406, 1019
Neiner C. et al., 2003b, A&A, 411, 565
Neiner C., Hubert A.-M., Frémat Y., Floquet M., Jankov S., Preuss O., Henrichs H. F., Zorec J., 2003c, A&A, 409, 275
Neiner C., Grunhut J. H., Petit V., ud-Doula A., Wade G. A., 2012a, MNRAS, 426, 2738
Neiner C., Landstreet J. D., Alecian E., Owocki S. P., Kochukhov O., Bohlender D. A., the MiMeS Collaboration, 2012b, A&A, 546, 44
Neiner C., Alecian E., Briquet M., Floquet M., Frémat Y., Martayan C., Thizy O. the MiMeS Collaboration, 2012c, A&A, 537, A148
Oksala M. E., Wade G. A., Townsend R. H. D., Owocki S. P., Kochukhov O., Neiner C., Alecian E., Grunhut J., 2012, MNRAS, 419, 959
Oskinova L. M., Todt H., Ignace R., Brown J. C., Cassinelli J. P., Hamann W.-R., 2011, MNRAS, 416, 1456
Pedersen H., 1979, A&AS, 35, 313
Petit V., 2011, in Neiner C., Wade G., Meynet G., Peters G., eds, IAU Symp. Vol. 272, Active OB Stars: Structure, Evolution, MassLoss, and Critical Limits. Cambridge Univ. Press, Cambridge, p. 208
Petit V., Wade G. A., 2012, MNRAS, 420, 773
Petit V., Wade G. A., Drissen L., Montmerle T., Alecian E., 2008, MNRAS, 387, L23
Petit V., Massa D. L., Marcolino W. L. F., Wade G. A., Ignace R., 2011, MNRAS, 412, L45
Petit V., Gagne M., Cohen D. H., Townsend R. H. D., Leutenegger M. A., Savoy M. R., Fehon G., Cartagena C. A., 2012, in Carciofi A., Rivinius T., eds, ASP Conf. Ser. Circumstellar Dynamics at High Resolution, Astron. Soc. Pac., San Francisco, in press (arXiv 1205.3538)
Preston G. W., 1967, ApJ, 150, 547
Puls J., Springmann U., Lennon M., 2000, A&AS, 141, 23
Puls J., Urbaneja M. A., Venero R., Repolust T., Springmann U., Jokuthy A., Mokiem M. R., 2005, A&A, 435, 669
Puls J., Vink J. S., Najarro F., 2008, A&AR, 16, 209
Raassen A. J. J., Cassinelli J. P., Miller N. A., Mewe R., Tepedelenlioğlu E., 2005, A&A, 437, 599
Raassen A. J. J., van der Hucht K. A., Miller N. A., Cassinelli J. P., 2008, A&A, 478, 513
Ramírez S. V. et al., 2004, AJ, 128, 787
Reed C., 2005, VizieR Online Data Catalog, 5125
Repolust T., Puls J., Herrero A., 2004, A&A, 415, 349
Rivinius T., Stahl O., Baade D., Kaufer A., 2003, Information Bull. Var. Stars, 5397, 1
Rivinius T., Hummel C. A., Stahl O., 2011, in Neiner C., Wade G., Meynet G., Peters G., eds, IAU Symp. Vol. 272, Active OB Stars: Structure, Evolution, MassLoss, and Critical Limits. Cambridge Univ. Press, Cambridge, p. 539
Rivinius T., Townsend R. H. D., Kochukhov O., Štefl S., Baade D., Barrera L., Szeifert T., 2012, MNRAS, in press
Romanyuk I. I., Kudryavtsev D. O., 2008, Astrophys. Bull., 63, 139
Runacres M. C., Owocki S. P., 2002, A&A, 381, 1015
Sanz-Forcada J., Franciosini E., Pallavicini R., 2004, A&A, 421, 715
Shore S. N., Brown D. N., 1990, ApJ, 365, 665
Shore S. N., Bohlender D. A., Bolton C. T., North P., Hill G. M., 2004, A&A, 421, 203
Shultz M. et al., 2012, ApJ, 750, 2
Silvester J. et al., 2009, MNRAS, 398, 1505
Simón-Díaz S., 2010, A&A, 510, A22
Simón-Díaz S., Herrero A., Esteban C., Najarro F., 2006, A&A, 448, 351
Simón-Díaz S., García-Rojas J., Esteban C., Stasińska G., López-Sánchez A. R., Morisset C., 2011, A&A, 530, A57
Stahl O., Wade G., Petit V., Stober B., Schanne L., 2008, A&A, 487, 323
Stelzer B., Flaccomio E., Montmerle T., Micela G., Sciortino S., Favata F., Preibisch T., Feigelson E. D., 2005, ApJS, 160, 557
Stibbs D. W. N., 1950, MNRAS, 110, 395
Sundqvist J. O., Puls J., Feldmeier A., Owocki S. P., 2011, A&A, 528, A64
Sundqvist J. O., ud-Doula A., Owocki S. P., Townsend R. H. D., Howarth I. D., Wade G. A., 2012, MNRAS, 423, L21
Townsend R. H. D., Owocki S. P., 2005, MNRAS, 357, 251
Townsend R. H. D., Owocki S. P., Groote D., 2005, ApJ, 630, L81
Townsend R. H. D., Owocki S. P., ud-Doula A., 2007, MNRAS, 382, 139
Townsend R. H. D., Oksala M. E., Cohen D. H., Owocki S. P., ud-Doula A., 2010, ApJ, 714, L318
Townsend R. H. D. et al., 2012, ApJ, submitted
Turner D. G., 1990, PASP, 102, 1331
ud-Doula A., 2008, in Hamann W.-R., Feldmeier A., Oskinova L. M., eds, Clumping in Hot-Star Winds. Electronic publication of the University Potsdam, p. 125
ud-Doula A., Owocki S. P., 2002, ApJ, 576, 413
ud-Doula A., Owocki S. P., Townsend R. H. D., 2008, MNRAS, 385, 97
ud-Doula A., Owocki S. P., Townsend R. H. D., 2009, MNRAS, 392, 1022
Uytterhoeven K., Harmanec P., Telting J. H., Aerts C., 2005, A&A, 440, 249
van Leeuwen F., 2007, A&A, 474, 653
Vink J. S., de Koter A., Lamers H. J. G. L. M., 2000, A&A, 362, 295
Vink J. S., de Koter A., Lamers H. J. G. L. M., 2001, A&A, 369, 574
Wade G. A., Bohlender D. A., Brown D. N., Elkin V. G., Landstreet J. D., Romanyuk I. I., 1997, A&A, 320, 172
Wade G. A., Bagnulo S., Kochukhov O., Landstreet J. D., Piskunov N., Stift M. J., 2001, A&A, 374, 265
Wade G. A., Fullerton A. W., Donati J.-F., Landstreet J. D., Petit P., Strasser S., 2006, A&A, 451, 195
Wade G. A. et al., 2011a, in Neiner C., Wade G., Meynet G., Peters G., eds, IAU Symp. Vol. 272, Active OB Stars: Structure, Evolution, MassLoss, and Critical Limits. Cambridge Univ. Press, Cambridge, p. 118
Wade G. A. et al., 2011b, MNRAS, 416, 3160
Wade G. A. et al., 2012a, MNRAS, 425, 1278
Wade G. A. et al., 2012b, MNRAS, 419, 2459
Walborn N. R., 1975, PASP, 87, 613
Walborn N. R., Nichols J. S., 1994, ApJ, 425, L29
Wang J., Townsley L. K., Feigelson E. D., Broos P. S., Getman K. V., Román-Zúñiga C. G., Lada E., 2008, ApJ, 675, 464
Weber E. J., Davis L. Jr, 1967, ApJ, 148, 217
Wolff S. C., 1990, AJ, 100, 1994
Wolff S. C., Strom S. E., Hillenbrand L. A., 2004, ApJ, 601, 979
Yakunin I., Romanyuk I., Kudryavtsev D., Semenko E., 2011, Astron. Nachr., 332, 974
Zacharias N., Monet D. G., Levine S. E., Urban S. E., Gaume R., Wycoff G. L., 2005, VizieR Online Data Catalog, 1297
Zboril M., North P., 2000, Contr. Astron. Observatory Skalnate Pleso, 30, 12
Zboril M., North P., Glagolevskij Y. V., Betrix F., 1997, A&A, 324, 949

APPENDIX A: NOTES ON INDIVIDUAL STARS

This section contains additional remarks about certain stars, marked by a dagger in Table 1, concerning our choice of parameters, providing alternative calculation in case of disagreements in the literature, or specific information about binarity and other relevant characteristics. The sections are numbered according to the ID number of each stars, as given in Column 1 of Table 1.

A3 HD 37022 (θ^1 Ori C)

θ^1 Ori C is a single-lined spectroscopic and astrometric binary with an 11-yr period and $e \approx 0.6$ (Kraus et al. 2009).

A4 HD 191612

HD 191612 is a double-lined spectroscopic binary with $P = 1548$ d and $e = 0.5$, and an early B-type companion (Howarth et al. 2007; Wade et al. 2011b).

A6 HD 47129 (Plaskett's star)

Plaskett's star is a high-mass ($M_{\rm tot} \sin i = 93 M_\odot$) O+O double-lined spectroscopic binary with a short period ($P = 14$ d) circular orbit (Linder et al. 2008). The magnetic field is associated with the rapidly rotating ($v \sin i = 300$ km s^{-1}) secondary star (Grunhut et al. 2012b).

A8 ALS 15218 (Tr 16-22)

We use the effective temperature and luminosity derived from the cluster photometry analysis of Gagné et al. (2011). We assume $\log(g) = 4.0$.

A10 HD 37742 (ζ Ori Aa)

HD 37742 is an astrometric double-lined spectroscopic binary (Hummel et al. 2000) with a O9 Ib primary and an early B-type star companion. The preliminary dynamic mass derived by Rivinius, Hummel & Stahl (2011) ($2.48 \pm 5.6\ M_\odot$) is smaller than the mass derived by Bouret et al. (2008) ($39 \pm 8\ M_\odot$).

A comparison of the disentangled component spectra with the published Zeeman magnetic signature confirms that the signature cannot originate from component Ab, since its lines are too narrow (Rivinius, private communication).

A12 HD 37061 (NU Ori)

NU Ori is a double-lined spectroscopic binary with $P = 19$ d and $e = 0.14$ (Abt, Wang & Cardona 1991), with a magnetic early B-type primary and a late B-type companion (Petit et al. 2008).

A18 HD 205021 (β Cep)

β Cep is a double-lined spectroscopic binary. The magnetic primary (component A) is the prototype of a class of pulsating hot stars. The secondary (component Aa) is an Hα-emitting classical Be star (Catanzaro 2008).

A19 ALS 15211 (Tr16-13)

We use the effective temperature and luminosity derived from the cluster photometry analysis of Gagné et al. (2011). We assume $\log(g) = 4.0$.

A20 HD 122451 (β Cen)

β Cen is a double-lined spectroscopic binary with $P = 356$ d and $e = 0.8$ (Ausseloos et al. 2006), and components of nearly identical mass. The magnetic field detection is associated with the narrow-line primary star (Alecian et al. 2011).

A24 HD 96446 (V 430 Car)

Matthews & Bohlender (1991) observed photometric variations with a period of 0.85 d, as well as other shorter periods interpreted as β Cep-type pulsations. However, other photometric periods are possible and compatible with the low-amplitude variations of the longitudinal field measurements (Neiner et al. 2012b). We use the long period of 5.73 d. The shortest period of 0.85 d would yield $W = 0.46$ and $R_{\rm K} = 1.7 R_*$.

A30 HD 37017 (V 1046 Ori)

V 1046 Ori is a double-lined spectroscopic binary with a 18.6 d period ($e = 0.4$). The field detection is associated with the B2 He-strong primary (Bolton et al. 1998). The companion is a late B-type star.

A32 HD 149277

An inspection of archival HARPS and MiMeS ESPaDonS spectra revealed that HD 149277 is a double-lined spectroscopic binary with the magnetic field detection associated with the lower $v \sin i$ component (Petit et al., in preparation).

A34 HD 37776 (V 901 Ori)

We choose the temperature and luminosity from Landstreet et al. (2007) in order to be consistent with the radius used by Kochukhov et al. (2011) in their magnetic analysis. Kochukhov et al. (2011) have shown that the field structure is much more complex than a dipole. Their surface magnetic field reconstruction displays a surface field varying from 5 kG to 30 kG across the stellar surface (see their fig. 4). As their associated mean magnetic field modulus varies between 13 and 16 kG, we use a dipolar strength of 15 kG to estimate the wind confinement. It is important to keep in mind that the resulting magnetospheric structure will be complex, and cannot be described in detail by a global $R_{\rm A}$, as testified by the complex Hα variations (Shultz et al., in preparation).

A35 HD 136504 (ϵ Lup)

ϵ Lup is an eccentric double-lined spectroscopic binary ($P = 4.6$ d, $e = 0.28$; Uytterhoeven et al. 2005), with similar components. The magnetic field measurements found in the literature (Hubrig et al. 2009; Shultz et al. 2012) do not specify which component is magnetic, but follow-up MiMeS observations show that the field is associated with the primary star and that the published longitudinal field measurements are underestimated by a factor of 2.

Uytterhoeven et al. (2005) also found a possible period of 1.2 d for the primary. This would lead to $W = 0.38$ and $R_{\rm K} = 1.9 R_*$.

A40 HD 186205

The SIMBAD data base gives a spectral type of B5, although Walborn (1975) classified it as B2Vp He-strong. The effective temperature determinations are varied: 17 kK (Zboril & North 2000) and 23.5 kK (Lee & Obrien 1977). An analysis of a MiMeS observation suggests $T_{\rm eff} = 20$ kK and $\log g = 4.0$.

A42 HD 200775 (V 3780 Cep)

HD 200775 is a double-lined spectroscopic binary with a period $\sim$4 yr ($e = 0.3$) with components of similar temperatures. The

magnetic field is associated with the sharp-lined primary star (Alecian et al. 2008a).

A48 HD 58260

According to the various parameter determinations reported by Cidale et al. (2007) and Bohlender (1989), we opt for $T_{\rm eff} = 20$ kK and $\log g = 3.55$.

Pedersen (1979) reports a possible period of 1.657 d, based on spectrophotometry of the HeI λ4026 Å line, with a variation of the order of 0.01 mag. Bychkov et al. (2005) phased the dozen available longitudinal field measurements with this period; however the amplitude of the variation is relatively small. We therefore use the $v \sin i$ as the lower limit on the equatorial velocity. The 1.6-d period, if confirmed, would yield $W = 0.55$ and $R_{\rm K} = 1.5R_*$, and an inclination angle of the rotation axis near zero.

A49 HD 36485 (δ Ori C)

δ Ori C is a double-lined spectroscopic binary with a 30-d period ($e = 0.32$). Leone et al. (2010) determined $T_{\rm eff} = 20$ kK and $M = 7\ {\rm M}_\odot$ for the magnetic primary, and $T_{\rm eff} = 10$ kK and $M = 2.8\ {\rm M}_\odot$ for the secondary star (with a ΔV difference of 1.3 mag).

Leone et al. (2010) determined a dipolar field strength between 7.3 and 12 kG. We use a mean value of 10 kG for our calculations.

A50 HD 208057 (16 Peg)

The star was reported once to display Hα emission (Merrill & Burwell 1943), but there exists no confirmation of this emission (Henrichs et al. 2009).

A52 HD 25558 (40 Tau)

A magnetic field detection was reported by Hubrig et al. (2009), but was refuted by Bagnulo et al. (2012) based on a re-analysis of the same data set. However, a weaker field was detected with MiMeS observations.

A53 HD 35298

Although Bychkov et al. (2005) reported a longitudinal field with extremum at 3 kG, Yakunin et al. (2011) found some larger values up to 5 kG but also reported large variation in the field determined with lines from different elements. The photometric period used by Bychkov et al. (2005) was confirmed by additional longitudinal field measurements at the Dominion Astrophysical Observatory, with an extremum around 5 kG (Bohlender, private communication). We opt for a conservative lower limit on the dipolar strength of 9 kG.

A55 HD 142990 (V 913 Sco)

There are many different effective temperature determinations in the literature, ranging from 16.5 to 18.5 kK (e.g. Cidale et al. 2007). We use 17.5 kK as a mean value and assume $\log(g) = 4.0$.

A56 HD 37058 (V 359 Ori)

Glagolevskij et al. (2007) determined $T_{\rm eff} = 17$ kK and $\log(g) = 3.80$ from spectral fitting. Landstreet et al. (2007) found a higher temperature of 20 kK. We, however, prefer the lower temperature given that the star is He-weak.

A period of 14 d was reported by Pedersen (1979) based on spectrophotometry of He lines. On the other hand, Bychkov et al. (2005) phased the sparse longitudinal field measurements from the literature with a period of 1.022 d. An additional measurement was taken by Bagnulo et al. (2006), but the period is not precise enough to test the phasing. We therefore use the conservative 14 d period. The shorter period would lead to $W = 0.57$ and $R_{\rm K} = 1.5R_*$.

A57 HD 35502

HD 35502 is a hierarchical spectroscopic triple system with a broad-lined magnetic B-type primary (HD 35502 A) and a companion (HD 35502 Bab) composed of two sharp-lined A-type stars (Bohlender et al., in preparation). Borra (1981) lists a possible period of 1.7 d; however this period is not compatible with the new longitudinal field measurements ($P = 0.85$ d).

A60 HD 61556 (HR 2949)

HD 61555/6 is a visual pair, the light of which is combined in the *Hipparcos* identifier HIP 37229 (Rivinius et al. 2003). Both components were observed separately in the context of the MiMeS Project, and a magnetic field was detected only for HD 61556.

A61 HD 175362 (Wolff's star)

There is a large scatter of effective temperature determinations in the literature, from 14 to 17 kK. We adopt the temperature ($T_{\rm eff} = 15$ kK) derived by Leone & Manfre (1997) and $\log g = 4.0$.

A62 HD 105382 (HR 4618)

Although often classified at a Be star, Briquet et al. (2001) have shown that this is not the case and the Be classifications probably resulted from accidentally observing the very nearby, well-known Be star δ Cen.

This paper has been typeset from a TEX/LATEX file prepared by the author.